applied sciences

MDPI

Article

Microstructural Length-Scale Effects on Shaped-Charge Jet Formation and Critical Liner Thickness: An Anisotropic Thermoviscoplastic Modeling Study

Wanqian Yu [1,2], Qianli Ma [3], Wenhao Yue [4,5], Sihan Zhao [2], Long Ji [2,*], Haijun Zhang [2], Hao Wang [4,5,*], Zhida Huang [4,5], Huming Liao [4,5], Yanhong Yang [4,5], Shaohua Jin [1] and Bo Li [3]

1 School of Materials Science and Engineering, Beijing Institute of Technology, Beijing 100081, China
2 National Key Laboratory of Land and Air Based Information Perception and Control, Xi'an Modern Control Technology Research Institute, Xi'an 710065, China
3 School of Mechanics and Engineering Science, Peking University, Beijing 100871, China
4 Xi'an Zhonglang Intelligent Control Technology Co., Ltd., Xi'an 710075, China
5 ESCAAS Co., Ltd., Jiaxing 314050, China
* Correspondence: jilong1683@163.com (L.J.); hao.wang@escaas.com.cn (H.W.)

Abstract

This study develops a thermoviscoplastic model that incorporates an effective through-thickness microstructural length into the Hill48 yield criterion for shaped-charge liners. The model is implemented in the axisymmetric Hot Optimal Transportation Meshfree (HOTM) framework and verified through directional-yield and material-coordinate transformation tests. An isotropic bulk reference is adopted to isolate the thickness-dependent directional correction in comparisons with conventional J2 plasticity. Comparison with a published experiment supports the predicted global jet-formation response, while independent validation of the microstructural mechanism remains necessary. For the representative numerical case, the proposed model predicts higher jet-tip velocity, greater jet length, and modified deformation localization. A Walsh-type plastic-instability criterion is used to bracket the critical liner thickness for three charge calibers. The nominal critical thickness increases with caliber, whereas its normalized value decreases, indicating a departure from proportional scaling within the investigated range. These results demonstrate the sensitivity of the predicted jet response to the assumed thickness-dependent constitutive description. The findings remain limited to the adopted phenomenological parameters and investigated configurations and do not establish a general scaling law. The framework provides a basis for subsequent material calibration and experimental validation.

Keywords: shaped-charge liner; plastic anisotropy; thermoviscoplastic constitutive model; Hill48 yield criterion; jet formation; scale effect

Check for updates

Academic Editor: Andrea Carpinteri

Received: 10 September 2026
Revised: 19 October 2026
Accepted: 22 October 2026
Published: 24 October 2026

Copyright: © 2026 by the authors. Licensee MDPI, Basel, Switzerland. This article is an open access article distributed under the terms and conditions of the Creative Commons Attribution (CC BY) license.

1. Introduction

Shaped-charge jet formation is a highly transient process in which a detonation wave drives a metallic liner to collapse toward the charge axis, producing a high-velocity jet and a relatively slow-moving slug [1–3]. These classical studies established the fundamental hydrodynamic description of liner collapse and jet–slug formation and provided the basis for subsequent analytical, experimental, and numerical investigations. During collapse, the liner experiences extremely high strain rates, large plastic deformation, rapid heating, material rotation, and complex stress-state evolution, making its constitutive response an

important factor governing collapse kinematics, material partitioning, jet velocity distribution, and final morphology [4,5]. Recent studies have further shown that detonation loading, liner geometry, material behavior, and the numerical treatment of large deformation can significantly affect jet formation and stretching [6–8]. Jet performance therefore depends not only on tip velocity, but also on the continuity and stability of the stretching jet, which may be degraded by nonuniform collapse, necking, and lateral disturbances [9]. These issues are particularly relevant to large-caliber shaped charges, for which geometric enlargement changes the absolute liner thickness, deformation distance, inertia, and characteristic loading time, potentially leading to departures from ideal geometric similitude [10]. Moreover, material-scale effects associated with the liner microstructure do not necessarily scale proportionally with the charge geometry. Reliable simulation of large-caliber shaped-charge jets therefore requires an accurate description of both the extreme thermomechanical response and the scale-dependent material behavior of the liner.

At the material level, such scale-dependent behavior is closely associated with the polycrystalline microstructure of the liner. Grain size, morphology, crystallographic texture, and grain-boundary characteristics are strongly influenced by the manufacturing process and can affect deformation compatibility, localization, and failure under intense dynamic loading. Jiang et al. showed that variations in the microstructure and grain size of copper shaped-charge liners can influence jet stretching and penetration through changes in flow stress, strain-rate sensitivity, and surface roughening [11]. Different manufacturing routes have likewise been reported to affect jet coherence and stretching through their influence on liner microstructure [12,13]. More generally, studies of metallic foils and thin sheets have revealed pronounced thickness-dependent variations in flow stress, plastic anisotropy, yield behavior, and strain localization when the material thickness approaches the underlying microstructural scale [14–17]. These observations suggest that the through-thickness response of shaped-charge liners may exhibit significant microstructure-related anisotropy, which should be considered in constitutive descriptions of liner collapse and jet formation.

Because such anisotropy is difficult to characterize directly under explosive loading, numerical simulation provides a practical means of examining its influence on liner collapse and jet formation. In modern hydrocodes, the volumetric response is generally described by an equation of state, while the deviatoric response is represented by a dynamic strength model. The Johnson–Cook model is widely used for its simple treatment of strain hardening, strain-rate strengthening, and thermal softening [5,6,18], while other models, including Steinberg–Cochran–Guinan, Zerilli–Armstrong, mechanical-threshold-stress, and Preston–Tonks–Wallace, have also been developed for high-rate and high-temperature deformation [19–22]. However, most shaped-charge simulations still employ an isotropic von Mises yield surface, and microstructural effects are commonly introduced only through scalar strength or failure parameters [11,23]. Although anisotropic criteria such as Hill48 can describe directional yielding [24], and manufacturing-induced anisotropy has been considered for specific liners [25], studies of spin-formed copper liners have shown that the anisotropic response depends strongly on local crystallographic texture and forming history [26,27]. Such texture-induced anisotropy may exhibit non-orthotropic features, including normal–shear coupling, so the corresponding parameters are specific to the manufacturing state rather than universal material constants. Nevertheless, most continuum formulations treat these directional parameters as fixed properties without explicitly linking them to liner thickness or an underlying microstructural length scale. Under geometric scaling, the liner thickness changes, whereas the underlying material characteristic scale does not necessarily vary proportionally; thus, geometric similarity does not necessarily imply constitutive similarity [10,28]. A constitutive framework explicitly linking liner thickness, microstructural length scale, and directional plastic response is therefore needed.

To address this limitation, the present study develops a microstructural-length-scale-dependent anisotropic thermoviscoplastic model for shaped-charge liner collapse and jet formation. An effective through-thickness microstructural characteristic length, ℓ_t, is introduced to phenomenologically represent the combined influence of grain size, morphology, texture, and grain-boundary constraints, and the relative material scale is characterized by $\Lambda_t = t_0/\ell_t$. The key distinction from conventional Hill48 formulations is that the through-thickness plastic resistance depends explicitly on the normalized thickness Λ_t, thereby incorporating the finite-thickness microstructural effect directly into the yield surface. The anisotropic formulation is combined with strain hardening, strain-rate strengthening, and thermal softening, while the high-pressure volumetric response is described separately by an equation of state. Building upon the previously developed HOTM framework and its axisymmetric extension [29–31], the model is implemented in the local material coordinate system of the liner and verified through directional-yield and coordinate-transformation tests. It is then applied to large-caliber shaped charges to compare the predicted jet-forming response with that of the conventional isotropic J2 model and to investigate the effects of liner thickness and charge caliber on jet stability and critical liner thickness.

2. Microstructural-Length-Scale-Dependent Anisotropic Thermoviscoplastic Model

2.1. Axisymmetric Kinematics and Local Material Coordinates

The shaped-charge configurations considered in this study are rotationally symmetric with respect to the charge axis in terms of the explosive geometry, liner geometry, initiation condition, and prescribed material properties. The dominant liner-collapse and jet-formation processes can therefore be represented in the meridional r-z plane under the assumption of axisymmetry, substantially reducing the computational cost while retaining the principal deformation mechanisms.

Under axisymmetric kinematics, all field variables are independent of the circumferential coordinate θ, and the circumferential velocity vanishes as

$$\frac{\partial(\,\cdot\,)}{\partial\theta} = 0, \qquad u_\theta = 0. \tag{1}$$

It should be emphasized that this spatial reduction does not imply a two-dimensional material response. Circumferential deformation, hoop stress, and the associated directional plastic resistance remain nonzero and are retained in the constitutive formulation.

To describe the anisotropic plastic response of the liner, an orthonormal local material basis $\{\boldsymbol{a}_1, \boldsymbol{a}_2, \boldsymbol{a}_3\}$ is defined at each material point, as illustrated in Figure 1. Here, $\boldsymbol{a}_1$ denotes the meridional tangent direction of the liner, $\boldsymbol{a}_2$ is the circumferential direction, and $\boldsymbol{a}_3$ denotes the through-thickness direction normal to the liner surface. Let $\{\boldsymbol{e}_r, \boldsymbol{e}_\theta, \boldsymbol{e}_z\}$ denote the cylindrical basis and α the angle between $\boldsymbol{a}_1$ and the radial direction. The local material basis is then expressed as

$$\boldsymbol{a}_1 = \cos\alpha\,\boldsymbol{e}_r + \sin\alpha\,\boldsymbol{e}_z, \tag{2}$$

$$\boldsymbol{a}_2 = \boldsymbol{e}_\theta, \tag{3}$$

$$\boldsymbol{a}_3 = -\sin\alpha\,\boldsymbol{e}_r + \cos\alpha\,\boldsymbol{e}_z. \tag{4}$$

Accordingly, the transformation matrix from the local material basis to the cylindrical basis is

$$\boldsymbol{Q}_c = \begin{bmatrix} \cos\alpha & 0 & -\sin\alpha \\ 0 & 1 & 0 \\ \sin\alpha & 0 & \cos\alpha \end{bmatrix}, \tag{5}$$

where the columns of $\boldsymbol{Q}_c$ correspond to $\boldsymbol{a}_1$, $\boldsymbol{a}_2$, and $\boldsymbol{a}_3$, respectively.

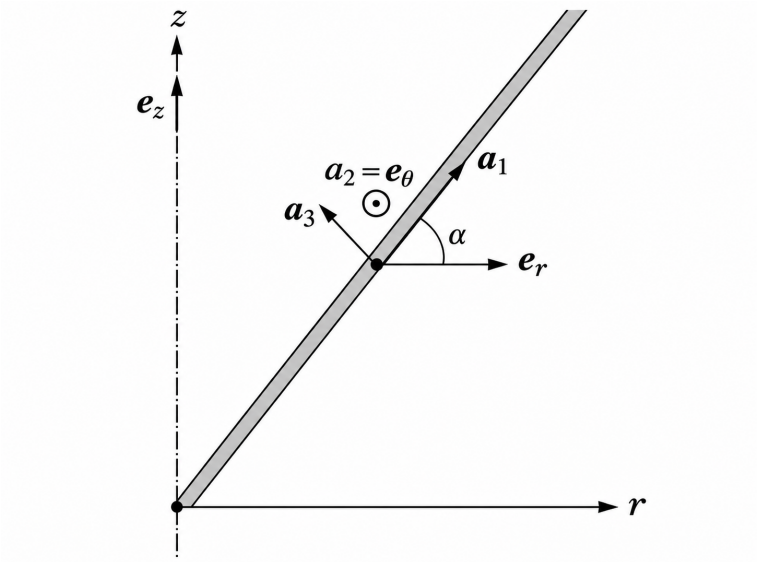


Figure 1. Cylindrical and local material coordinate systems of the shaped-charge liner. Here, $\boldsymbol{a}_1$, $\boldsymbol{a}_2$, and $\boldsymbol{a}_3$ represent the meridional, circumferential, and through-thickness directions, respectively.

A second-order tensor can then be transformed between the cylindrical and local material coordinates as

$$\boldsymbol{\sigma}^m = \boldsymbol{Q}_c^T \boldsymbol{\sigma} \boldsymbol{Q}_c, \qquad \boldsymbol{\sigma} = \boldsymbol{Q}_c \boldsymbol{\sigma}^m \boldsymbol{Q}_c^T, \tag{6}$$

where the superscript m denotes quantities expressed in the local material coordinate system. The same transformation is applied to other second-order tensors required by the constitutive model.

The local material basis is initialized from the undeformed liner geometry and subsequently updated with the material motion during liner collapse. The anisotropic constitutive equations are always evaluated in this local coordinate system. Details of the orientation update and its implementation within the axisymmetric HOTM framework are given in Section 3.

2.2. Local State Variables and Elastic Response

Let (R, Z) and (r, z) denote the material coordinates in the reference and current configurations, respectively, with the corresponding material points denoted by $\boldsymbol{X}(R, Z)$ and $\boldsymbol{x}(r, z)$. Under axisymmetric deformation, the deformation gradient is written as

$$\boldsymbol{F} = \hat{\nabla}_0 \boldsymbol{\varphi} = \begin{bmatrix} \dfrac{\partial r}{\partial R} & 0 & \dfrac{\partial r}{\partial Z} \\ 0 & \dfrac{r}{R} & 0 \\ \dfrac{\partial z}{\partial R} & 0 & \dfrac{\partial z}{\partial Z} \end{bmatrix}, \tag{7}$$

where $\boldsymbol{\varphi}$ denotes the deformation mapping and $\hat{\nabla}_0$ is the gradient operator with respect to the reference configuration. The local thermomechanical state is characterized by the deformation gradient $\boldsymbol{F}$, the internal variables $\boldsymbol{Z}$, the temperature T, and the thermal driving variable, which is defined as

$$\boldsymbol{G} = -\frac{1}{T} \hat{\nabla} T. \tag{8}$$

Following the multiplicative decomposition proposed by Lee [32], the deformation gradient is decomposed into elastic and plastic parts as

$$\boldsymbol{F} = \boldsymbol{F}^e \boldsymbol{F}^p, \tag{9}$$

where $\boldsymbol{F}^e$ and $\boldsymbol{F}^p$ denote the elastic and plastic deformation gradients, respectively. The Helmholtz free energy is decomposed into volumetric elastic, deviatoric elastic, plastic-storage, and thermal contributions as

$$A = W^{e,\mathrm{vol}}(J,T) + W^{e,\mathrm{dev}}(\boldsymbol{F}\boldsymbol{F}^{p-1},T) + W^{p}(\boldsymbol{F}^{p},T) + W^{h}(T), \tag{10}$$

where $J = \det \boldsymbol{F}$. The thermal contribution is taken as

$$W^{h}(T) = C(T)\left(T - T_0 - T\log\frac{T}{T_0}\right), \tag{11}$$

where $C(T)$ is the temperature-dependent specific heat capacity per unit reference volume and T_0 is the reference temperature.

The high-pressure volumetric response is described by the Mie–Grüneisen equation of state [33–37] as

$$p = \begin{cases} (\gamma_0 + b\mu)E + \dfrac{\rho_0 C_0^2 \mu\left[1 + \left(1 - \frac{\gamma_0}{2}\right)\mu - \frac{b}{2}\mu^2\right]}{\left[1 - (S_1 - 1)\mu - S_2\frac{\mu^2}{\mu+1} - S_3\frac{\mu^3}{(\mu+1)^2}\right]^2}, & \mu > 0, \\ \rho_0 C_0^2 \mu + \gamma_0 E, & \mu \le 0, \end{cases} \tag{12}$$

where the compression measure is defined as

$$\mu = \frac{\rho}{\rho_0} - 1. \tag{13}$$

Here, p is the pressure, ρ_0 and ρ are the reference and current densities, C_0 is the reference bulk sound speed, and E is the internal energy per unit reference volume. The coefficients S_1, S_2, and S_3 describe the shock-velocity–particle-velocity relation, whereas γ_0 and b are the Grüneisen parameters.

The deviatoric elastic response is expressed as

$$W^{e,\mathrm{dev}} = G(T)\left\|\boldsymbol{\epsilon}^{e,\mathrm{dev}}\right\|^2, \tag{14}$$

where the temperature-dependent shear modulus is given by

$$G(T) = \frac{G_t}{1 + \exp[a(T - T_c)]}, \tag{15}$$

with G_t, a, and T_c determined from material data. The deviatoric elastic logarithmic strain is defined as

$$\boldsymbol{\epsilon}^{e,\mathrm{dev}} = \frac{1}{2}\log\left(J^{-2/3}\boldsymbol{F}^{eT}\boldsymbol{F}^{e}\right). \tag{16}$$

2.3. Anisotropic Hill48 Yield Criterion

To describe the directional plastic response of the liner, the Hill48 anisotropic yield criterion [24] is adopted. The constitutive evaluation is performed in the local material coordinate system defined in Section 2.1, where directions 1, 2, and 3 correspond to the meridional, circumferential, and through-thickness directions, respectively. In this coordinate system, the Hill48 quadratic form is written as

$$\begin{aligned} \Phi = {} & F^{\mathrm{H}}\left(\sigma_{22}^{m} - \sigma_{33}^{m}\right)^2 + G^{\mathrm{H}}\left(\sigma_{33}^{m} - \sigma_{11}^{m}\right)^2 + H^{\mathrm{H}}\left(\sigma_{11}^{m} - \sigma_{22}^{m}\right)^2 \\ & + 2L^{\mathrm{H}}\left(\sigma_{23}^{m}\right)^2 + 2M^{\mathrm{H}}\left(\sigma_{31}^{m}\right)^2 + 2N^{\mathrm{H}}\left(\sigma_{12}^{m}\right)^2, \end{aligned} \tag{17}$$

where F^{H}, G^{H}, H^{H}, L^{H}, M^{H}, and N^{H} are the dimensionless Hill48 coefficients. The corresponding equivalent stress is defined as

$$\bar{\sigma}_{\mathrm{H}} = \sqrt{\Phi}. \tag{18}$$

The yield function is then expressed as

$$f = \bar{\sigma}_{\mathrm{H}} - \sigma_y\left(\bar{\varepsilon}^p, \dot{\bar{\varepsilon}}^p, T\right) \le 0, \tag{19}$$

where σ_y denotes the current thermoviscoplastic flow stress. The material response is elastic for $f < 0$, whereas plastic yielding occurs when $f = 0$. Since the Hill48 criterion depends only on stress differences and shear components, it is independent of hydrostatic pressure. The pressure response can therefore be described separately by the equation of state introduced in Section 2.2.

Under the present axisymmetric condition, the circumferential shear components vanish as

$$\sigma_{12}^m = \sigma_{23}^m = 0, \tag{20}$$

and the Hill equivalent stress reduces to

$$\bar{\sigma}_{\mathrm{H}}^2 = F^{\mathrm{H}}\left(\sigma_{22}^m - \sigma_{33}^m\right)^2 + G^{\mathrm{H}}\left(\sigma_{33}^m - \sigma_{11}^m\right)^2 + H^{\mathrm{H}}\left(\sigma_{11}^m - \sigma_{22}^m\right)^2 + 2M^{\mathrm{H}}\left(\sigma_{31}^m\right)^2. \tag{21}$$

Thus, only F^{H}, G^{H}, H^{H}, and M^{H} contribute to the axisymmetric constitutive response.

These coefficients are determined from the reference directional normal yield strengths σ_1^y, σ_2^y, and σ_3^y, together with the reference shear yield strength τ_{31}^y. Substitution of the corresponding uniaxial and pure-shear stress states into the Hill48 criterion gives

$$F^{\mathrm{H}} = \frac{1}{2}\left[\left(\frac{\sigma_{\mathrm{ref}}}{\sigma_2^y}\right)^2 + \left(\frac{\sigma_{\mathrm{ref}}}{\sigma_3^y}\right)^2 - \left(\frac{\sigma_{\mathrm{ref}}}{\sigma_1^y}\right)^2\right], \tag{22}$$

$$G^{\mathrm{H}} = \frac{1}{2}\left[\left(\frac{\sigma_{\mathrm{ref}}}{\sigma_3^y}\right)^2 + \left(\frac{\sigma_{\mathrm{ref}}}{\sigma_1^y}\right)^2 - \left(\frac{\sigma_{\mathrm{ref}}}{\sigma_2^y}\right)^2\right], \tag{23}$$

$$H^{\mathrm{H}} = \frac{1}{2}\left[\left(\frac{\sigma_{\mathrm{ref}}}{\sigma_1^y}\right)^2 + \left(\frac{\sigma_{\mathrm{ref}}}{\sigma_2^y}\right)^2 - \left(\frac{\sigma_{\mathrm{ref}}}{\sigma_3^y}\right)^2\right], \tag{24}$$

and

$$M^{\mathrm{H}} = \frac{1}{2}\left(\frac{\sigma_{\mathrm{ref}}}{\tau_{31}^y}\right)^2. \tag{25}$$

Here, σ_{ref} is a fixed reference stress used to normalize the directional yield strengths and define the shape of the anisotropic yield surface. It is distinct from the evolving thermoviscoplastic flow stress σ_y in Equation (19). The dependence of the directional yield strengths, and hence the Hill48 coefficients, on the through-thickness microstructural length scale is introduced in Section 2.6.

2.4. Thermoviscoplastic Flow Stress Model

The Hill48 criterion introduced in the preceding subsection defines the anisotropic shape of the yield surface, whereas its evolution during plastic deformation is governed by the current thermoviscoplastic flow stress σ_y. To account for the extreme deformation conditions encountered during liner collapse and jet formation, the thermoviscoplastic flow stress incorporating strain hardening, strain-rate strengthening, and thermal softening is expressed as

$$\sigma_y = \begin{cases} \sigma_0\left(1 + \dfrac{\bar{\varepsilon}^p}{\bar{\varepsilon}_0^p}\right)^{1/n}\left[1 + \left(\dfrac{\dot{\bar{\varepsilon}}^p}{\dot{\bar{\varepsilon}}_0^p}\right)^{1/m}\right]\left(1 - \dfrac{T - T_0}{T_m - T_0}\right)^l, & T < T_m, \\ 0, & T \ge T_m. \end{cases} \tag{26}$$

Here, σ_0 is the initial yield stress at the reference state, $\bar{\varepsilon}^p$ and $\dot{\bar{\varepsilon}}^p$ are the accumulated equivalent plastic strain and equivalent plastic strain rate, respectively, and $\bar{\varepsilon}_0^p$ and $\dot{\bar{\varepsilon}}_0^p$ are the

corresponding reference values. The parameters n, m, and l control the strain-hardening, strain-rate, and thermal-softening responses, respectively, while T_0 and T_m denote the reference and melting temperatures.

The accumulated equivalent plastic strain is defined as

$$\bar{\varepsilon}^p = \int_0^t \dot{\bar{\varepsilon}}^p \, \mathrm{d}t. \tag{27}$$

Combined with the Hill48 equivalent stress defined in Section 2.3, plastic yielding occurs when

$$\bar{\sigma}_{\mathrm{H}} = \sigma_y. \tag{28}$$

Accordingly, the Hill48 coefficients control the directional shape of the yield surface, whereas σ_y governs its evolution with plastic strain, strain rate, and temperature.

The plastic flow direction is determined using an associated flow rule in the local material coordinate system. Accordingly, the plastic rate-of-deformation tensor is given by

$$\mathbf{D}^{p,m} = \dot{\lambda} \frac{\partial f}{\partial \boldsymbol{\sigma}^m} = \dot{\lambda} \frac{\partial \bar{\sigma}_H}{\partial \boldsymbol{\sigma}^m}, \tag{29}$$

where $\dot{\lambda}$ is the non-negative plastic multiplier. The loading–unloading conditions are governed by the standard Kuhn–Tucker conditions as

$$\dot{\lambda} \geq 0, \qquad f \leq 0, \qquad \dot{\lambda} f = 0. \tag{30}$$

The equivalent plastic strain rate is defined consistently through plastic-work equivalence as

$$\sigma_y \dot{\bar{\varepsilon}}^p = \boldsymbol{\sigma}^m : \mathbf{D}^{p,m}, \tag{31}$$

so that the accumulated equivalent plastic strain entering the thermoviscoplastic flow-stress model is obtained from Equation (27).

2.5. Temperature Rise Induced by Plastic Dissipation

During liner collapse and jet formation, severe plastic deformation occurs over a very short time scale, and a substantial fraction of the plastic work is converted into heat. Because heat conduction is comparatively slow during this stage, the plastic deformation is treated as locally adiabatic. Consistent with the thermal energy definition in Section 2.2, the heat-generation rate associated with plastic dissipation is written as

$$C(T)\dot{T}_p = \beta J \, \boldsymbol{\sigma} : \mathbf{D}^p, \tag{32}$$

where $J = \det \mathbf{F}$ and β is the Taylor–Quinney coefficient. Using the plastic-work equivalence relation introduced in Section 2.4, the temperature-rise rate becomes

$$\dot{T}_p = \frac{\beta J \sigma_y \dot{\bar{\varepsilon}}^p}{C(T)}. \tag{33}$$

2.6. Microstructural-Length-Scale Modification of Through-Thickness Yield Strength

The Hill48 formulation introduced above provides a general description of anisotropic yielding through the directional normal and shear yield strengths. To account for microstructure-related thickness effects without explicitly resolving individual grains, an effective through-thickness microstructural characteristic length, ℓ_t, is introduced. This quantity represents, in a phenomenological sense, the combined influence of grain size, morphology, crystallographic texture, grain-boundary constraints, and their spatial correlations, and should therefore not be interpreted as the mean grain size itself.

The relative scale between the liner thickness and the underlying microstructure is characterized by

$$\Lambda_t = \frac{t_0}{\ell_t}, \tag{34}$$

where t_0 is the initial liner thickness. A smaller value of Λ_t corresponds to a stronger influence of the finite microstructural scale, whereas the response gradually approaches its bulk-material limit as Λ_t increases.

The anisotropic plastic response of a liner depends on its manufacturing-induced microstructure, including deformation history, crystallographic texture, grain morphology, and grain-boundary arrangement. Even under the same material and manufacturing conditions, the effective directional response may vary with liner thickness. Because the through-thickness dimension is much smaller than the in-plane dimensions, thickness changes alter the number of grain layers or effective microstructural units across the liner. Grain boundaries, local microstructural constraints, and free surfaces are therefore expected to affect the through-thickness response more strongly, whereas the larger in-plane dimensions are expected to approach the bulk-material limit more readily.

Accordingly, the thickness-dependent correction is applied to the through-thickness normal yield strength, while manufacturing-induced anisotropy is represented by the directional yield strengths in the Hill48 framework. A bounded transition function is defined as

$$\chi_t(\Lambda_t) = 1 - \frac{A_t}{1 + (\Lambda_t/\Lambda_0)^p}. \tag{35}$$

The effective characteristic length ℓ_t represents the microstructural scale relevant to the through-thickness response rather than the mean grain size alone. It may be constrained experimentally by through-thickness grain dimensions and grain-boundary spacing, grain-layer number, grain morphology and aspect ratio, and crystallographic orientation correlations. The parameters A_t, Λ_0, and p control the maximum strength deviation from the bulk limit, the normalized transition thickness, and the transition sharpness, respectively. The scale-dependent through-thickness yield strength is then expressed as

$$\sigma_3^y(\Lambda_t) = \chi_t(\Lambda_t)\, \sigma_{3,\infty}^y, \tag{36}$$

where $\sigma_{3,\infty}^y$ denotes the through-thickness yield strength in the bulk-material limit. The remaining directional strengths, σ_1^y, σ_2^y, and τ_{31}^y, retain their general anisotropic values in the present formulation. The variation of the correction factor with the normalized thickness is illustrated in Figure 2, showing the transition from the finite microstructural-scale regime to the bulk anisotropic response.

The correction function satisfies

$$\lim_{\Lambda_t \to \infty} \chi_t(\Lambda_t) = 1, \tag{37}$$

and

$$\lim_{\Lambda_t \to 0} \chi_t(\Lambda_t) = 1 - A_t. \tag{38}$$

Thus, the proposed modification is bounded and gradually vanishes as the liner thickness becomes sufficiently large relative to the characteristic microstructural length. The formulation therefore recovers the conventional bulk anisotropic response rather than predicting an unbounded variation of strength with liner thickness.

Substituting Equation (36) into the Hill48 relations gives the scale-dependent coefficients

$$F^{\mathrm{H}}(\Lambda_t) = \frac{1}{2}\left[\left(\frac{\sigma_{\mathrm{ref}}}{\sigma_2^y}\right)^2 + \left(\frac{\sigma_{\mathrm{ref}}}{\sigma_3^y(\Lambda_t)}\right)^2 - \left(\frac{\sigma_{\mathrm{ref}}}{\sigma_1^y}\right)^2\right], \tag{39}$$

$$G^{\mathrm{H}}(\Lambda_t) = \frac{1}{2}\left[\left(\frac{\sigma_{\mathrm{ref}}}{\sigma_3^y(\Lambda_t)}\right)^2 + \left(\frac{\sigma_{\mathrm{ref}}}{\sigma_1^y}\right)^2 - \left(\frac{\sigma_{\mathrm{ref}}}{\sigma_2^y}\right)^2\right], \tag{40}$$

$$H^{\mathrm{H}}(\Lambda_t) = \frac{1}{2}\left[\left(\frac{\sigma_{\mathrm{ref}}}{\sigma_1^y}\right)^2 + \left(\frac{\sigma_{\mathrm{ref}}}{\sigma_2^y}\right)^2 - \left(\frac{\sigma_{\mathrm{ref}}}{\sigma_3^y(\Lambda_t)}\right)^2\right], \tag{41}$$

$$M^{\mathrm{H}} = \frac{1}{2}\left(\frac{\sigma_{\mathrm{ref}}}{\tau_{31}^y}\right)^2. \tag{42}$$

A physically interpretable calibration requires independent microstructural characterization and thickness-dependent mechanical measurements. EBSD, metallography, or related measurements can constrain ℓ_t using the microstructural quantities described above. For specimens with different thicknesses but consistent material and processing conditions, the through-thickness yield strength can then be normalized by its corresponding bulk-limit value to calibrate A_t, Λ_0, and p. When expressed in terms of the physical thickness t_0, the correction law depends on the combined scale $\ell_t\Lambda_0$. Thus, thickness-dependent strength data alone cannot generally identify ℓ_t and Λ_0 independently; microstructural characterization of ℓ_t or an external constraint on either parameter is required.

The proposed modification is a phenomenological continuum representation of microstructure-related thickness effects rather than an explicit grain-scale model. The thickness-dependent correction is restricted to the through-thickness normal resistance as a first-order approximation, motivated by the smaller dimension and finite number of grain layers or effective microstructural units in this direction. This does not exclude scale effects in the meridional, circumferential, or shear responses, which may be incorporated when sufficient direction-dependent experimental data become available.

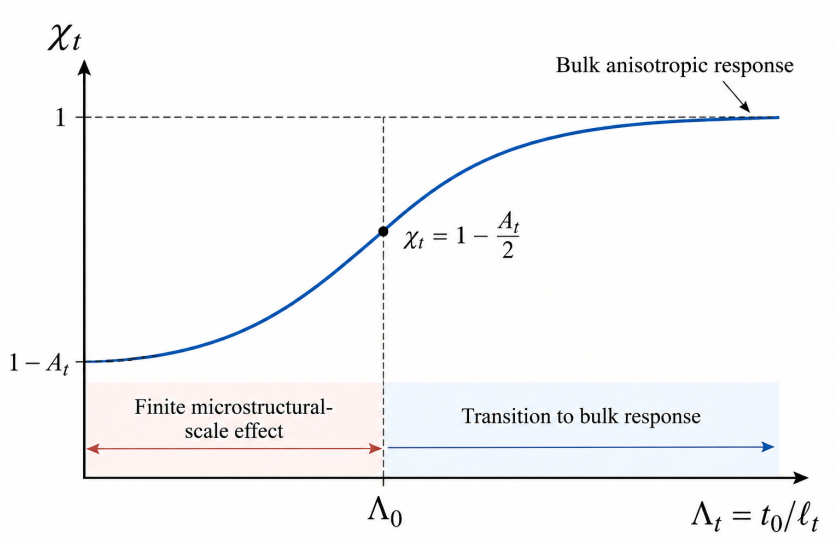


Figure 2. Schematic variation of the through-thickness correction factor χ_t with the normalized thickness $\Lambda_t = t_0/\ell_t$. The scale-dependent effect gradually decays with increasing Λ_t, and the response approaches the bulk anisotropic limit as $\chi_t \to 1$.

3. Numerical Implementation and Constitutive Verification in the Axisymmetric HOTM Framework

3.1. Overview of the Axisymmetric HOTM Framework

The constitutive model developed in the preceding section is implemented within the previously developed Hot Optimal Transportation Meshfree (HOTM) framework and its axisymmetric extension [29–31]. To improve reproducibility, the governing discrete equations and principal implementation details relevant to the present calculations are summarized below.

HOTM combines an optimal-transport-based time discretization [38] with a variational formulation of dissipative thermomechanics [39,40] in a unified Lagrangian meshfree framework. It has been applied to strongly nonlinear thermomechanical problems involving large deformation, contact, friction, material interaction, and fracture [41–48], making it well suited to the severe collapse and stretching encountered during shaped-charge jet formation. Under axisymmetry, the three-dimensional body is represented by its meridional section, while circumferential deformation and hoop stress are retained. The local constitutive response therefore remains three-dimensional.

The thermomechanical evolution in HOTM is governed by a variational principle. The local material state is characterized by the deformation gradient $\boldsymbol{F}$, internal variables $\boldsymbol{Z}$, and temperature T. The Helmholtz free-energy density $A(\boldsymbol{F}, \boldsymbol{Z}, T)$ describes the recoverable thermomechanical response, while viscous deformation, internal-variable evolution, and heat conduction are represented by the dissipation potentials ϕ^*, ψ^*, and χ, respectively. The resulting variational functional is written as

$$\begin{aligned}\Phi = &\int_{\Omega_0}\left[\dot{K} + \dot{A} + \eta\dot{T} + \phi^* + \psi^* - \chi\right]\mathrm{d}V - \int_{\Omega_0}\rho_0\boldsymbol{B}\cdot\dot{\boldsymbol{\varphi}}\,\mathrm{d}V - \int_{\Gamma_t}\overline{\boldsymbol{T}}\cdot\dot{\boldsymbol{\varphi}}\,\mathrm{d}A \\ &+ \int_{\Omega_0}\rho_0 Q\log\left(\frac{T}{T_0}\right)\mathrm{d}V - \int_{\Gamma_q}\bar{h}\log\left(\frac{T}{T_0}\right)\mathrm{d}A,\end{aligned} \tag{43}$$

where K is the kinetic-energy density, $\eta = -\partial A/\partial T$ is the entropy density, ρ_0 is the reference density, $\boldsymbol{B}$ is the body force, $\overline{\boldsymbol{T}}$ is the prescribed traction, Q is the volumetric heat source, and $\bar{h}$ is the prescribed boundary heat flux. The thermal driving variable associated with heat conduction is

$$\boldsymbol{G} = -\frac{1}{T}\nabla_0 T. \tag{44}$$

The governing equations and corresponding boundary conditions follow from the stationarity condition

$$\inf_{\dot{\boldsymbol{\varphi}}}\sup_{T}\inf_{\dot{\boldsymbol{Z}}}\Phi(\dot{\boldsymbol{\varphi}}, T, \dot{\boldsymbol{Z}}). \tag{45}$$

For a time interval $[t_n, t_{n+1}]$, the continuous variational problem is recast as the following incremental problem

$$\Phi_n\left[\boldsymbol{\varphi}_{n+1}, T_{n+1}, \boldsymbol{Z}_{n+1}\right] = \inf_{\text{path}}\int_{t_n}^{t_{n+1}}\Phi\,\mathrm{d}t. \tag{46}$$

The inertial contribution is discretized using the Wasserstein-distance-based optimal-transport formulation, while the energetic, dissipative, and thermal contributions are treated within the corresponding incremental variational framework. Consistent with the axisymmetric HOTM implementation [31], the non-inertial contributions are evaluated using a backward-Euler time discretization. The mechanical, thermal, and constitutive states at t_{n+1} are then obtained from the first-order optimality conditions.

For spatial discretization, the meridional domain is represented by nodes and material points. The nodes carry the primary kinematic and thermal variables, whereas the material points store the constitutive state variables and material properties and serve as quadrature

points. In practice, the initial nodal and material-point distributions are generated from a finite-element-type partition of the meridional domain: the element vertices are used as HOTM nodes and the corresponding quadrature or center points are initialized as material points. The initial element connectivity is used only for initialization and is not retained during the subsequent HOTM calculation. Under axisymmetry, the integration weight associated with material point p is

$$w_p = 2\pi r_p s_p, \tag{47}$$

where r_p is the radial coordinate and s_p is the represented area in the meridional plane. The factor $2\pi r_p$ accounts for the circumferential contribution. The kinematic and thermal fields are approximated using local maximum-entropy (LME) shape functions [49] as

$$\boldsymbol{\varphi}^h = \sum_a N_a \boldsymbol{\varphi}_a, \qquad T^h = \sum_a N_a T_a. \tag{48}$$

The node–material-point support is updated during deformation, allowing the discretization to accommodate the severe distortion associated with liner collapse and jet stretching. Specifically, the local nodal neighborhood associated with each material point is reconstructed as the material evolves, so that the approximation is not constrained by a permanently connected mesh topology.

The spatially discretized variational equations yield the following nodal mechanical and thermal balance equations

$$\boldsymbol{f}_a^{\text{int}} - \boldsymbol{f}_a^{\text{ext}} = m_a \ddot{\boldsymbol{\varphi}}_a, \tag{49}$$

and

$$Q_a^{\text{int}} - Q_a^{\text{ext}} = 0, \tag{50}$$

where $\boldsymbol{f}_a^{\text{int}}$ and $\boldsymbol{f}_a^{\text{ext}}$ denote the internal and external mechanical forces, respectively, and Q_a^{int} and Q_a^{ext} are the corresponding thermal contributions. The thermal equation is consistent with the continuum energy balance

$$T\dot{\eta} = \boldsymbol{P}^v : \dot{\boldsymbol{F}} + \boldsymbol{Y}^d \cdot \dot{\boldsymbol{Z}} - \hat{\nabla}_0 \cdot \boldsymbol{q} + \rho_0 Q, \tag{51}$$

where $\boldsymbol{P}^v : \dot{\boldsymbol{F}}$ and $\boldsymbol{Y}^d \cdot \dot{\boldsymbol{Z}}$ represent viscous and internal-variable dissipation, respectively, and $\boldsymbol{q}$ denotes the heat flux. Thus, mechanical dissipation, thermal evolution, and heat conduction are incorporated within the same variational framework.

For the axisymmetric mechanical problem, the circumferential contribution enters explicitly into the radial internal force as

$$f_a^{r,\text{int}} = \sum_p w_p \left[P_{rr} N_{a,r} + P_{rz} N_{a,z} + \frac{N_a}{r_p} (P_{rr} - P_{\theta\theta}) \right], \tag{52}$$

whereas the axial contribution is

$$f_a^{z,\text{int}} = \sum_p w_p \left[P_{rz} N_{a,r} + P_{zz} N_{a,z} \right]. \tag{53}$$

The term $N_a(P_{rr} - P_{\theta\theta})/r_p$ represents the hoop-stress contribution and distinguishes the axisymmetric formulation from the corresponding planar two-dimensional form.

Because the axisymmetric equations contain geometric terms proportional to $1/r$, special treatment is required near the symmetry axis. Radial displacement and velocity are constrained to zero on the axis, which also acts as a rigid non-penetrating boundary for nodes and material points [31].

For material points near the axis, a weighted radius-regularization scheme is employed. The near-axis region is defined by

$$\Omega_{\text{axis}} = \{ \boldsymbol{x} \in \Omega \mid r \le r_c \}, \qquad r_c = \alpha h, \tag{54}$$

where h is the characteristic nodal spacing and $\alpha = 0.5$ is adopted in the present calculations. Within this region, an effective radius is introduced as

$$r_{\text{eff}} = \sqrt{r^2 + r_0^2}, \qquad r_0 = \eta h, \tag{55}$$

with $\eta = 0.1$. To recover the standard axisymmetric formulation smoothly away from the axis, the physical and effective radii are blended according to

$$\bar{r} = [1 - w(r)]r + w(r)r_{\text{eff}}, \tag{56}$$

where

$$w(r) = \begin{cases} \left(1 - \dfrac{r}{r_c}\right)^2, & r < r_c, \\ 0, & r \geq r_c. \end{cases} \tag{57}$$

Accordingly, the singular geometric factors are evaluated using

$$\frac{1}{r} \longrightarrow \frac{1}{\bar{r}} \tag{58}$$

Within the near-axis region, an effective radius is blended with the physical radius to regularize the singular geometric terms, as defined in Equations (54)–(58). This localized treatment recovers the standard axisymmetric formulation outside the regularization region. The adopted regularization parameters follow the sensitivity assessment in Ref. [31]. Artificial bulk viscosity is additionally employed to suppress spurious pressure oscillations under strong shock loading.

With the above axis constraints, radius regularization, dynamically reconstructed support domains, and shock stabilization, the principal implementation features used in the present axisymmetric calculations are specified explicitly rather than being delegated solely to the previous axisymmetric study. The resulting framework retains the thermomechanical consistency and large-deformation capability of HOTM while providing an efficient numerical basis for the anisotropic shaped-charge simulations considered in this study. Further implementation details used in the optimal-transport time-integration algorithm, dynamic support-domain reconstruction, artificial viscosity stabilization, and contact treatment are provided in Ref. [31] and are not repeated here for brevity.

3.2. Local Material Coordinate Transformation for Anisotropic Plasticity

The anisotropic constitutive model is formulated in the local material coordinate system of the liner, whereas the axisymmetric HOTM equations are solved in the cylindrical coordinate system. Since the liner undergoes large rotation during collapse and jet formation, the material orientation must be updated continuously so that the anisotropic response remains associated with the instantaneous meridional, circumferential, and through-thickness directions.

The initial material basis $\{\boldsymbol{a}_1^0, \boldsymbol{a}_2^0, \boldsymbol{a}_3^0\}$ is constructed from the undeformed liner geometry as defined in Section 2.1. During deformation, the current meridional direction is updated using the deformation gradient as

$$\boldsymbol{a}_1 = \frac{\boldsymbol{F}\boldsymbol{a}_1^0}{\|\boldsymbol{F}\boldsymbol{a}_1^0\|}, \tag{59}$$

while the circumferential direction remains

$$\boldsymbol{a}_2 = \boldsymbol{e}_\theta. \tag{60}$$

The current through-thickness direction is then reconstructed from

$$\boldsymbol{a}_3 = \boldsymbol{a}_1 \times \boldsymbol{a}_2. \tag{61}$$

The corresponding orthogonal transformation matrix is

$$\boldsymbol{Q}_{\mathrm{c}} = \begin{bmatrix} \boldsymbol{a}_1 & \boldsymbol{a}_2 & \boldsymbol{a}_3 \end{bmatrix}, \tag{62}$$

where the basis vectors are expressed in the current cylindrical coordinate system.

Before the constitutive update, the stress tensor is transformed from the cylindrical frame to the local material frame according to

$$\boldsymbol{\sigma}^m = \boldsymbol{Q}_{\mathrm{c}}^T \boldsymbol{\sigma} \boldsymbol{Q}_{\mathrm{c}}. \tag{63}$$

Under axisymmetry, both the global and local stress tensors retain the reduced form

$$\boldsymbol{\sigma} = \begin{bmatrix} \sigma_{rr} & 0 & \sigma_{rz} \\ 0 & \sigma_{\theta\theta} & 0 \\ \sigma_{rz} & 0 & \sigma_{zz} \end{bmatrix}, \qquad \boldsymbol{\sigma}^m = \begin{bmatrix} \sigma_{11}^m & 0 & \sigma_{13}^m \\ 0 & \sigma_{22}^m & 0 \\ \sigma_{13}^m & 0 & \sigma_{33}^m \end{bmatrix}. \tag{64}$$

The Hill48 yield criterion and the thermoviscoplastic update are then evaluated entirely in the local material coordinate system using the formulation described in Section 2.3. In particular, the microstructural length-scale correction introduced in Section 2.6 remains associated with the instantaneous through-thickness direction $\boldsymbol{a}_3$. Thus, although the liner may undergo large rotation, the scale-dependent directional resistance follows the material orientation rather than remaining aligned with the fixed cylindrical coordinates.

After the constitutive update, the stress tensor is transformed back to the cylindrical coordinate system as

$$\boldsymbol{\sigma} = \boldsymbol{Q}_{\mathrm{c}} \boldsymbol{\sigma}^m \boldsymbol{Q}_{\mathrm{c}}^T, \tag{65}$$

and is subsequently transferred to the axisymmetric HOTM mechanical calculation. This transformation procedure ensures a consistent coupling between the evolving liner orientation and the anisotropic constitutive response throughout collapse and jet formation.

3.3. Verification of the Microstructural-Length-Scale-Dependent Anisotropic Response

This subsection verifies the length-scale-dependent anisotropic yield surface and the transformation between cylindrical and local material coordinates. To isolate these effects, strain hardening, strain-rate strengthening, and thermal softening are suppressed, with the current flow stress fixed at the reference value, $\sigma_y = \sigma_{\mathrm{ref}}$.

The parameters used in this subsection are listed in Table 1. They are selected only to produce a sufficiently pronounced anisotropic and length-scale-dependent response for verification and do not represent calibrated properties of a specific shaped-charge liner material. The values used here are selected solely for constitutive verification and are not identical to those adopted in the shaped-charge calculations in the following section.

Table 1. Parameters used for constitutive verification.

$\boldsymbol{\sigma_{\mathrm{ref}}}$ (MPa)	$\boldsymbol{\sigma_1^y}$ (MPa)	$\boldsymbol{\sigma_2^y}$ (MPa)	$\boldsymbol{\sigma_{3,\infty}^y}$ (MPa)	$\boldsymbol{\tau_{31}^y}$ (MPa)	$\boldsymbol{A_t}$ –	$\boldsymbol{\Lambda_0}$ –	$\boldsymbol{p}$ –
300	300	315	330	180	0.25	40	2

The first test considers a single material point under homogeneous uniaxial loading in the $\boldsymbol{a}_1 - \boldsymbol{a}_3$ plane. The loading direction is

$$\boldsymbol{n} = \cos\psi\, \boldsymbol{a}_1 + \sin\psi\, \boldsymbol{a}_3, \tag{66}$$

where ψ is measured from the meridional material direction. For the uniaxial stress state $\boldsymbol{\sigma}^{\mathrm{m}} = \sigma\, \boldsymbol{n} \otimes \boldsymbol{n}$, the nonzero material stress components are

$$\sigma_{11}^m = \sigma \cos^2\psi, \qquad \sigma_{33}^m = \sigma \sin^2\psi, \qquad \sigma_{13}^m = \sigma \sin\psi \cos\psi, \tag{67}$$

with $\sigma_{22}^{m} = 0$. The corresponding Hill48 equivalent stress can be written as

$$\bar{\sigma}_{\mathrm{H}}^{2} = \sigma^{2} C_{\mathrm{H}}(\psi, \Lambda_t), \tag{68}$$

where

$$\begin{aligned} C_{\mathrm{H}}(\psi, \Lambda_t) = {} & F^{\mathrm{H}}(\Lambda_t) \sin^4 \psi + G^{\mathrm{H}}(\Lambda_t) \left(\sin^2 \psi - \cos^2 \psi\right)^2 \\ & + H^{\mathrm{H}}(\Lambda_t) \cos^4 \psi + 2M^{\mathrm{H}} \sin^2 \psi \cos^2 \psi. \end{aligned} \tag{69}$$

The analytical directional yield strength is therefore

$$\sigma_{\mathrm{dir}}^{y}(\psi, \Lambda_t) = \frac{\sigma_{\mathrm{ref}}}{\sqrt{C_{\mathrm{H}}(\psi, \Lambda_t)}}. \tag{70}$$

The verification is performed for $\Lambda_t = 10$, 40, and 80, together with the bulk limit $\Lambda_t \to \infty$, over $0^\circ \le \psi \le 90^\circ$. The numerical results are compared with Equation (70) in Figure 3. At the principal directions, the analytical solution satisfies

$$\sigma_{\mathrm{dir}}^{y}(0^\circ, \Lambda_t) = \sigma_{1}^{y}, \qquad \sigma_{\mathrm{dir}}^{y}(90^\circ, \Lambda_t) = \sigma_{3}^{y}(\Lambda_t), \tag{71}$$

so that the through-thickness response directly reflects the prescribed length-scale correction, while the intermediate angles verify its consistent propagation through the Hill48 yield surface.

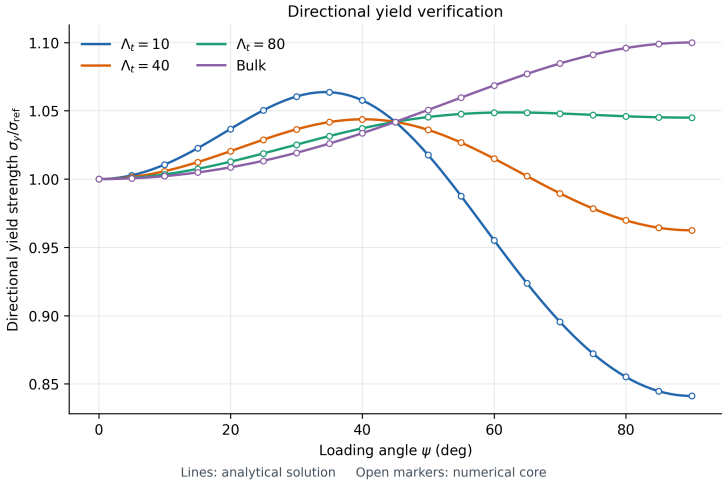


Figure 3. Verification of the directional yield response for different normalized thicknesses Λ_t. Numerical results are compared with the analytical Hill48 solution, including the bulk anisotropic limit.

The second test verifies the coordinate transformation. Let the local meridional direction form an angle α with the global radial direction, while the loading direction forms an angle β. Their relative orientation is

$$\psi = \beta - \alpha. \tag{72}$$

A fixed value of $\psi = 30^\circ$ is used, while α is varied from 0° to 90° and $\beta = \alpha + 30^\circ$. Although the global stress components vary with α, the transformed material components should remain

$$\frac{\sigma_{11}^{m}}{\sigma} = 0.75, \qquad \frac{\sigma_{33}^{m}}{\sigma} = 0.25, \qquad \frac{\sigma_{13}^{m}}{\sigma} = 0.4330. \tag{73}$$

Figure 4 presents the coordinate-transformation verification. Figure 4a shows the normalized stress components expressed in the global cylindrical coordinates, which vary continuously as the material basis rotates. After transformation into the local material

system, the corresponding components shown in Figure 4b remain invariant at the analytical values determined by the fixed relative loading angle $\psi = 30^\circ$.

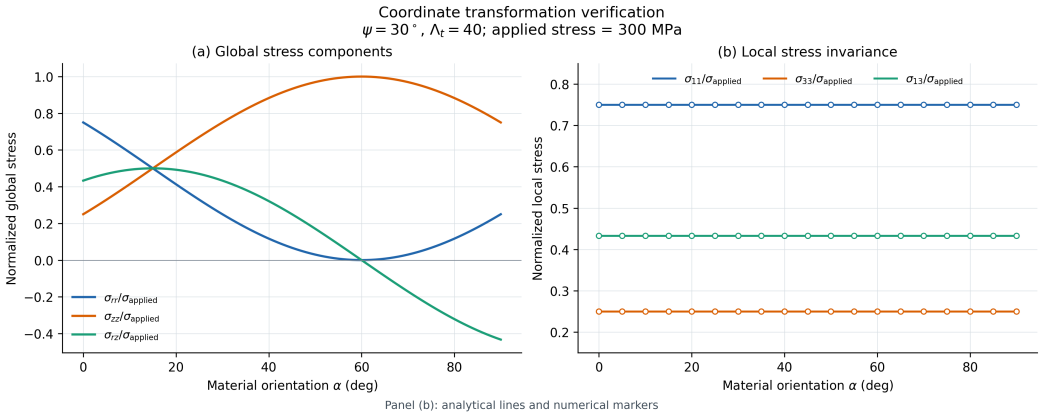


Figure 4. Verification of the local material-coordinate transformation for a fixed relative loading angle $\psi = 30^\circ$. The normalized material stress components remain invariant as the material basis rotates relative to the global cylindrical coordinates.

These two material-point tests verify the length-scale-dependent anisotropic response and the associated coordinate-transformation procedure used in the axisymmetric HOTM implementation.

3.4. Experimental Validation of Shaped-Charge Jet Formation

The copper-liner shaped-charge experiment reported in Ref. [50] was reproduced using the geometry, material properties, and initiation condition specified in Figure 5. The proposed scale-dependent Hill48 model and the conventional J2 model used identical numerical settings and differed only in the liner constitutive description. No constitutive or numerical parameters were recalibrated against the validation measurements.

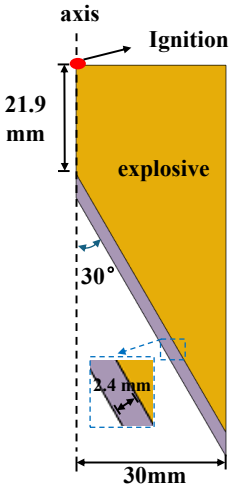


Figure 5. Geometry and numerical configuration of the copper-liner shaped-charge validation case reproduced according to Ref. [50]. Dimensions are given in millimeters.

Figure 6 compares the experimental and predicted jet configurations at $t = 36.5$ µs. Both models reproduce the overall jet morphology, with the proposed model showing closer agreement with the experimental configuration. Table 2 also shows smaller absolute relative errors for the proposed model in jet-tip velocity, jet-tail velocity, and jet length, reducing the mean absolute percentage deviation from 6.68% to 3.98%.

The largest discrepancy remains in jet-tail velocity, which may be affected by the explosive description, numerical resolution, and identification of the jet–slug transition. Overall, this benchmark supports the predicted global jet-formation response but does not independently validate the proposed microstructural length-scale mechanism.

Table 2. Comparison of the published experimental measurements and present numerical predictions for the copper-liner shaped charge.

Parameter	Experiment	Proposed	Relative Error (%)	J_2	Relative Error (%)
Tip velocity (m/s)	5534.6	5480.3	−0.98	5291.4	−4.39
Tail velocity (m/s)	1363.2	1249.9	−8.31	1208.5	−11.35
Jet length at 36.5 μs (mm)	67.6	65.8	−2.66	64.7	−4.29
Mean absolute percentage deviation (%)	—	3.98	—	6.68	—

Note: The relative error is defined as $(X_{num} - X_{exp})/X_{exp} \times 100\%$.

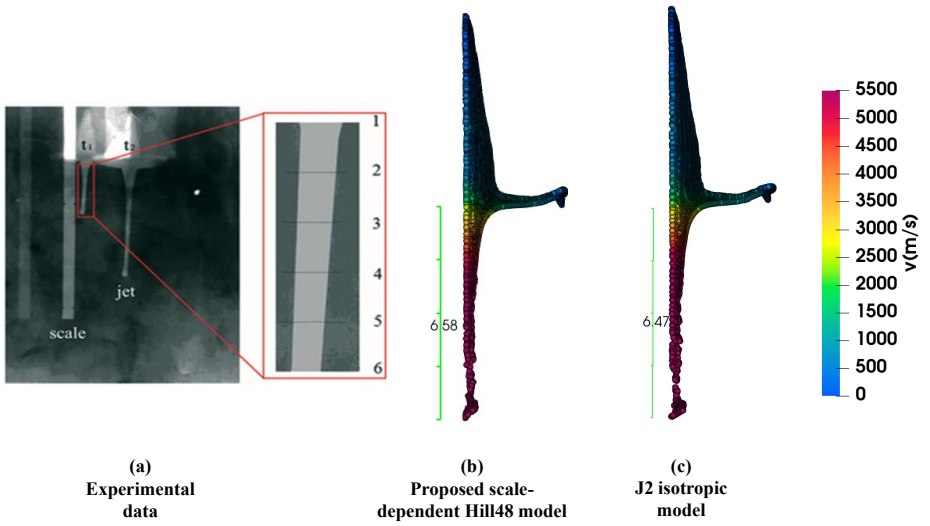


Figure 6. Comparison of the copper-jet configurations at $t = 36.5$ μs: (**a**) pulsed X-ray image reported in Ref. [50]; (**b**) numerical prediction obtained using the proposed scale-dependent model; and (**c**) numerical prediction obtained using the conventional J_2 model. Panels (**b**,**c**) are presented using the same spatial scale and axial reference position.

4. Microstructural Length-Scale Effects on Shaped-Charge Jet Formation and Critical Liner Thickness

4.1. Computational Configuration and Case Design for Large-Caliber Shaped Charges

4.1.1. Baseline Configuration and Numerical Settings

The proposed constitutive formulation is applied to a series of large-caliber shaped-charge simulations to investigate its influence on liner collapse, jet formation, and critical liner thickness. The axisymmetric configuration consists of a conical metallic liner, a cylindrical explosive charge, and rear-center initiation, as illustrated in Figure 7 for the representative case with $D = 300$ mm and $t_0 = 8$ mm. For different charge calibers, the liner cone angle is kept unchanged, while all geometric dimensions except the liner thickness are scaled proportionally with the charge caliber D. The liner and surrounding explosive are discretized using the same characteristic material-point spacing of 0.25 mm. The same numerical treatment, including the discretization strategy, contact treatment, explosive model, and boundary conditions, is otherwise employed for the corresponding simulations.

The principal numerical settings are summarized in Table 3 and used for all charge calibers unless otherwise stated. The local node–material-point neighborhoods are re-

constructed during deformation, while the initial quadrilateral partition does not impose fixed connectivity on the subsequent HOTM calculation. The near-axis treatment follows Section 3.1, with the adopted regularization parameters listed in Table 3.

For each caliber, the initial liner thickness t_0 is varied in increments of 0.5 mm around the transition between continuous and unstable jet formation. The effective through-thickness microstructural characteristic length is fixed at $\ell_t = 0.25$ mm for all cases, corresponding to the same liner material and manufacturing condition. The normalized thickness $\Lambda_t = t_0/\ell_t$, defined in Section 2.6, therefore varies only with t_0. It should be noted that ℓ_t is a constitutive characteristic length and is conceptually independent of the numerical material-point spacing, although the two quantities take the same value in the present calculations.

Table 3. Principal numerical settings used in the axisymmetric HOTM shaped-charge simulations.

Numerical Setting	Symbol/Treatment	Value/Specification
Coordinate formulation	–	Axisymmetric (r, z)
Liner material-point spacing	$h_{\mathrm{mp}}^{\mathrm{liner}}$	0.25 mm
Explosive material-point spacing	$h_{\mathrm{mp}}^{\mathrm{exp}}$	0.25 mm
LME locality parameter	γ	1.6
Near-axis activation radius	r_c	$0.5h$
Near-axis regularization length	r_0	$0.1h$
Axis boundary condition	–	$u_r = v_r = 0$ at $r = 0$
Axis non-penetration treatment	–	Rigid symmetry plane

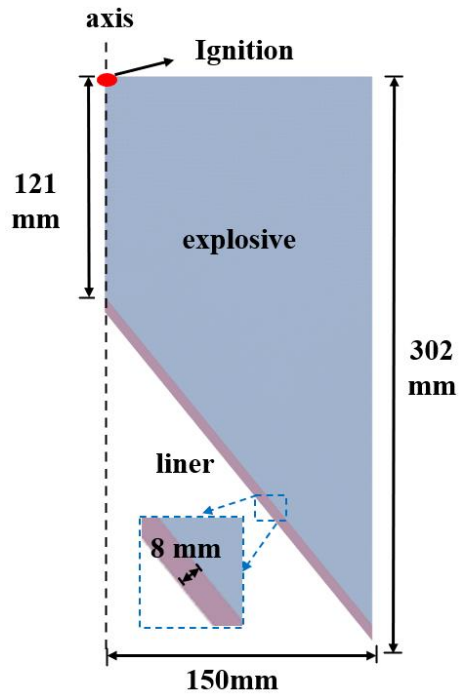


Figure 7. Representative geometry of the $D = 300$ mm, $t_0 = 8$ mm shaped-charge configuration.

The numerical study contains two parts. First, the representative configuration with $D = 300$ mm and $t_0 = 8$ mm is calculated using both the conventional isotropic J2 model and the proposed microstructural-length-scale-dependent anisotropic model. This comparison is used to evaluate the influence of the constitutive modification on liner collapse, jet kinematics, axial stretching, and local deformation under otherwise identical conditions. Second, a multi-caliber thickness sweep is performed for $D = 250$, 300, and 350 mm to identify the stable–unstable transition and determine the corresponding critical liner thickness for each caliber. The complete case matrix is summarized in Table 4.

Table 4. Case design for the multi-caliber shaped-charge simulations.

Group	Caliber D (mm)	Liner Thickness t_0 (mm)	$\Lambda_t = t_0/\ell_t$	Constitutive Model
S1	250	7.0	28	Proposed scale-dependent Hill48 model
		7.5	30	Proposed scale-dependent Hill48 model
		8.0	32	Proposed scale-dependent Hill48 model
		8.5	34	Proposed scale-dependent Hill48 model
		9.0	36	Proposed scale-dependent Hill48 model
S2	300	7.5	30	Proposed scale-dependent Hill48 model
		8.0	32	J2 Isotropic/Proposed scale-dependent Hill48 model
		8.5	34	Proposed scale-dependent Hill48 model
		9.0	36	Proposed scale-dependent Hill48 model
		9.5	38	Proposed scale-dependent Hill48 model
S3	350	8.5	34	Proposed scale-dependent Hill48 model
		9.0	36	Proposed scale-dependent Hill48 model
		9.5	38	Proposed scale-dependent Hill48 model
		10.0	40	Proposed scale-dependent Hill48 model
		10.5	42	Proposed scale-dependent Hill48 model

4.1.2. Spatial-Resolution Sensitivity

A spatial-resolution sensitivity analysis was performed for the standard case with $D = 300$ mm and $t_0 = 8$ mm. Three material-point spacings, $h = 0.500$, 0.250, and 0.125 mm, were considered while keeping the physical characteristic length fixed at $\ell_t = 0.250$ mm, giving $h/\ell_t = 2$, 1, and 0.5, respectively. All other material parameters, initial conditions, and numerical settings remained unchanged.

Figure 8 compares the jet-tip velocity histories. The maximum velocities are 5628, 5805, and 5942 m/s for the three spacings, respectively. Relative to the $h = 0.250$ mm baseline, the coarser and finer cases differ by 3.05% and 2.36%. The corresponding final jet lengths are 323.62, 334.36, and 348.83 mm, with relative differences of 3.21% and 4.32%. These results indicate limited spatial-resolution sensitivity; $h = 0.250$ mm is therefore retained to balance computational accuracy and efficiency.

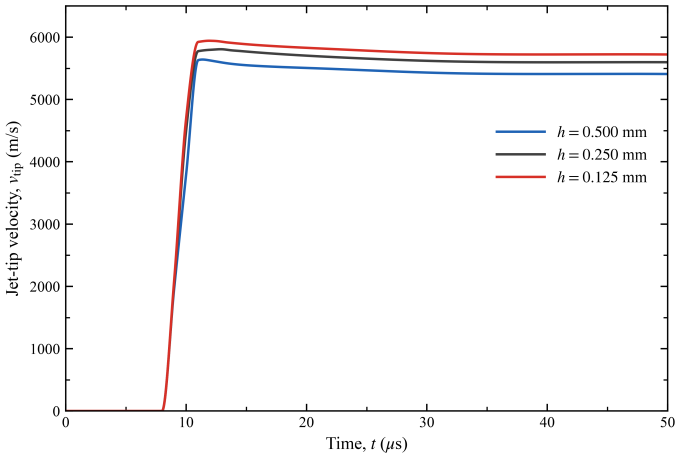


Figure 8. Effect of the material-point spacing on the jet-tip velocity for the standard case with $D = 300$ mm and $t_0 = 8$ mm. The physical characteristic length was fixed at $\ell_t = 0.250$ mm in all calculations.

The physical characteristic length ℓ_t enters the constitutive model through $\Lambda_t = t_0/\ell_t$ and does not determine the material-point spacing, support domain, or reconstruction parameters. Thus, its equality with h in the baseline case is coincidental rather than imposed. Varying h over a fourfold range at fixed ℓ_t produces modest changes in tip velocity and jet length, with no anomalous response at $h = \ell_t$, providing numerical support for their independence within the investigated resolution range.

4.2. Explosive and Liner Material Models

The shaped-charge simulations involve an energetic material providing the detonation loading and a metallic liner undergoing severe collapse and jet formation. The explosive is described using the previously developed thermo–mechanical–chemical formulation [51], whereas the liner employs the microstructural-length-scale-dependent anisotropic thermo-viscoplastic model developed in Section 2. The material parameters used in the present calculations are summarized at the end of this subsection.

4.2.1. Explosive Model

The explosive is represented by a two-phase mixture of unreacted solid explosive and gaseous reaction products. A reaction variable λ describes the local reaction progress, with $\lambda = 0$ and $\lambda = 1$ corresponding to the fully unreacted and fully reacted states, respectively. Following [51], both temperature- and pressure-driven reaction mechanisms are included. The temperature-dependent contribution is described by the following Arrhenius-type relation [52,53],

$$\left(\frac{d\lambda}{dt}\right)_T = A_{\mathrm{A}}(1-\lambda)\exp\left(-\frac{E_a}{RT}\right), \tag{74}$$

while the pressure-dependent contribution is represented by the Lee–Tarver Ignition and Growth (IG) model [54,55] as

$$\left(\frac{d\lambda}{dt}\right)_p = \mathcal{R}_I + \mathcal{R}_{G1} + \mathcal{R}_{G2}, \tag{75}$$

with the individual reaction-rate terms given by

$$\mathcal{R}_I = I(1-\lambda)^b\left(\frac{\rho}{\rho_0} - 1 - a\right)^x, \quad \lambda \le \lambda_{I,\max} \tag{76}$$

$$\mathcal{R}_{G1} = G_1(1-\lambda)^c\lambda^d p^y, \quad \lambda \le \lambda_{G1,\max} \tag{77}$$

$$\mathcal{R}_{G2} = G_2(1-\lambda)^e\lambda^g p^z, \quad \lambda \ge \lambda_{G2,\min}. \tag{78}$$

The total reaction rate is

$$\frac{d\lambda}{dt} = \left(\frac{d\lambda}{dt}\right)_T + \left(\frac{d\lambda}{dt}\right)_p. \tag{79}$$

Before reaction, the solid explosive retains both volumetric and deviatoric resistance. Its volumetric response is described by the Mie–Grüneisen equation of state, while the deviatoric response follows the thermoviscoplastic formulation in [51]. The reaction products are modeled using the Jones–Wilkins–Lee (JWL) equation of state [56–58] as

$$p_g = A_{\mathrm{JWL}}\left(1 - \frac{\omega\theta}{R_1}\right)\exp\left(-\frac{R_1}{\theta}\right) + B_{\mathrm{JWL}}\left(1 - \frac{\omega\theta}{R_2}\right)\exp\left(-\frac{R_2}{\theta}\right) + \omega\theta\rho_0 E, \tag{80}$$

where $\theta = \rho/\rho_0$. The mixture stress is obtained by combining the solid-phase stress with the pressure contribution of the reaction products [59] as

$$\boldsymbol{\sigma}_e = \boldsymbol{\sigma}_s - \lambda p_g \boldsymbol{I}. \tag{81}$$

Although the unified formulation contains both thermal and pressure-driven reaction mechanisms, the shaped-charge loading considered here is dominated by the rapid pressure-driven IG reaction following rear-center initiation. The Arrhenius contribution is retained for consistency with the unified explosive formulation, whereas the JWL pressure of the reaction products provides the principal loading responsible for liner collapse.

In the present shaped-charge simulations, the explosive is represented by a PBX 9501-like HMX-based polymer-bonded explosive. The constitutive, equation-of-state, and

reaction-rate parameters are adopted from representative data reported in the literature for PBX 9501 and its HMX constituent. In particular, the Ignition-and-Growth and detonation-product JWL parameters follow the PBX 9501 parameterization reported by Tarver et al. [60], while the Arrhenius thermal-reaction parameters are taken from the global PBX 9501 reaction-rate formulation reported by Menikoff [61]. The Mie–Grüneisen parameters used for the unreacted HMX solid phase are adopted from the data summarized by Wei et al. [62]. All parameters are converted to SI units and are listed in Table 5.

Table 5. Material and reaction parameters of the explosive used in the numerical simulations.

Parameter	Symbol	Value
Initial explosive state		
Initial PBX density	ρ_0	1910 kg/m^3
Initial temperature	T_0	298 K
Mie–Grüneisen EOS for the unreacted solid phase		
Bulk sound speed	c_0	2740 m/s
Hugoniot slope coefficient	s	2.60
Grüneisen coefficient	Γ_s	1.10
JWL EOS for detonation products		
JWL coefficient	A_{JWL}	1.6689×10^{12} Pa
JWL coefficient	B_{JWL}	5.969×10^{10} Pa
JWL exponent	R_1	5.90
JWL exponent	R_2	2.10
JWL Grüneisen coefficient	ω	0.45
Initial product energy density	E_0	9.5×10^9 J/m^3
Arrhenius thermal-reaction model		
Pre-exponential factor	A_{A}	5.6×10^{11} s^{-1}
Activation energy	E_a	1.49×10^5 J/mol
Universal gas constant	R	8.314 J/(mol K)
Ignition term		
Ignition coefficient	I	1.4×10^{17} s^{-1}
Compression threshold	a	0
Unreacted-fraction exponent	b	0.667
Compression exponent	x	20.0
First growth term		
First growth coefficient	G_1	1.30×10^{-14} Pa^{-2}s^{-1}
Unreacted-fraction exponent	c	0.667
Reacted-fraction exponent	d	0.277
Pressure exponent	y	2.0
Second growth term		
Second growth coefficient	G_2	4.00×10^{-14} Pa^{-2}s^{-1}
Unreacted-fraction exponent	e	0.333
Reacted-fraction exponent	g	1.0
Pressure exponent	z	2.0
Reaction-progress limits		
Maximum ignition reaction fraction	$\lambda_{I,\max}$	0.30
Maximum first-growth reaction fraction	$\lambda_{G1,\max}$	0.50
Minimum second-growth reaction fraction	$\lambda_{G2,\min}$	0.50

4.2.2. Liner Material and Microstructural Length Scale

The liner is described using the constitutive formulation presented in Section 2. The volumetric response is represented by the Mie–Grüneisen equation of state, whereas the deviatoric response incorporates strain hardening, strain-rate strengthening, thermal softening, and the microstructural-length-scale-dependent anisotropic yield criterion.

The general formulation in Section 2 permits arbitrary bulk anisotropy through independently specified directional yield strengths. However, sufficiently reliable direction-dependent data for the present liner material under the relevant manufacturing and loading conditions are unavailable. Although anisotropic parameters have been reported for specific spin-formed copper liners [26,27], they depend strongly on forming history, local texture, and sampling position. Transferring these parameters to the present liner without independent characterization would introduce uncontrolled manufacturing-specific anisotropy. The normalization stress is defined as

$$\sigma_{\mathrm{ref}} = \sigma_0, \tag{82}$$

and the bulk directional strengths are prescribed as

$$\sigma_1^y = \sigma_2^y = \sigma_{3,\infty}^y = \sigma_{\mathrm{ref}} = \sigma_0, \qquad \tau_{31}^y = \frac{\sigma_0}{\sqrt{3}}. \tag{83}$$

With these values, the Hill48 yield surface recovers the isotropic J2 response in the bulk limit. Thus, within the present controlled numerical study, the difference between the J2 and proposed formulations is associated with the scale-dependent modification of the through-thickness plastic resistance. This choice is specific to the present simulations and does not restrict the general anisotropic Hill48 formulation developed in Section 2. Accordingly, an additional fixed-anisotropy Hill48 baseline is not introduced in the present study, because assigning anisotropic coefficients without liner-specific experimental calibration would introduce uncontrolled manufacturing-dependent effects and obscure the isolated influence of the microstructural length-scale correction.

For the proposed model, the effective through-thickness microstructural characteristic length ℓ_t is kept constant for all cases corresponding to the same liner material and manufacturing condition. With the isotropic bulk reference defined above, the scale-dependent through-thickness yield strength follows Equation (36) as

$$\sigma_3^y(\Lambda_t) = \chi_t(\Lambda_t)\sigma_0. \tag{84}$$

As $\Lambda_t \to \infty$, $\chi_t \to 1$, and the proposed formulation therefore approaches the isotropic J2 bulk response adopted in the present simulations.

The liner material considered in the present study is OFHC copper. The conventional equation-of-state, elastic, thermal, and strength-related parameters are adopted from published data for OFHC copper or determined by matching the present thermoviscoplastic flow-stress formulation to the corresponding constitutive response reported in the literature [18,63,64]. In particular, the high-pressure equation-of-state parameters are based on commonly used Mie–Grüneisen data for copper, while the strain-hardening, strain-rate, and thermal-softening parameters of the present flow-stress model are selected to reproduce the representative high-rate response of OFHC copper reported by Johnson and Cook [18]. The resulting material parameters used in the shaped-charge calculations are summarized in Table 6. The microstructural-length-scale parameters in Table 6 are representative phenomenological values rather than independently calibrated constants for the present liner. In particular, ℓ_t represents an effective microstructural length rather than a measured mean grain size. A complete calibration dataset of the type described in Section 2.6 is currently

unavailable; the present parameterization is therefore used to investigate the consequences of the proposed thickness-dependent formulation.

Table 6. Thermomechanical and microstructural-scale parameters of the liner used in the shaped-charge simulations.

Parameter	Symbol	Value
Mie–Grüneisen equation of state		
Reference density	ρ_0	8960 kg/m^3
Bulk sound speed	c_0	3940 m/s
Hugoniot slope coefficient	S_1	1.489
Grüneisen coefficient	γ_0	2.02
Elastic and thermal properties		
Initial shear modulus	G_0	46.5 GPa
Poisson's ratio	ν	0.34
Reference temperature	T_0	298 K
Melting temperature	T_m	1356 K
Specific heat capacity	c_p	383 J/(kg K)
Taylor–Quinney coefficient	β_{TQ}	0.90
Thermoviscoplastic flow-stress model		
Initial/reference yield stress	$\sigma_0 = \sigma_{\mathrm{ref}}$	90 MPa
Reference plastic strain	$\bar{\epsilon}_0^p$	0.20
Strain-hardening parameter	n	1.40
Reference plastic strain rate	$\dot{\bar{\epsilon}}_0^p$	0.25 s^{-1}
Rate-sensitivity parameter	m	50
Thermal-softening exponent	l	0.90
Bulk Hill48 reference strengths		
Meridional reference yield strength	σ_1^y	90 MPa
Circumferential reference yield strength	σ_2^y	90 MPa
Bulk through-thickness reference yield strength	$\sigma_{3,\infty}^y$	90 MPa
Reference shear yield strength	τ_{31}^y	51.96 MPa
Bulk Hill48 coefficients	F^H, G^H, H^H, M^H	0.5, 0.5, 0.5, 1.5
Microstructural-length-scale correction		
Effective microstructural characteristic length	ℓ_t	0.25 mm
Maximum strength-reduction amplitude	A_t	0.30
Characteristic transition scale	Λ_0	50
Transition exponent	p	3.5

4.3. Comparison of Jet Formation Between the Isotropic J2 and Microstructural-Length-Scale-Dependent Models

To examine the influence of the proposed microstructural length-scale correction on liner collapse and jet formation, a representative large-caliber case is selected from the calculation matrix introduced in Section 4.1. The charge caliber and initial liner thickness are $D = 300$ mm and $t_0 = 8$ mm, respectively. With the effective through-thickness microstructural characteristic length $\ell_t = 0.25$ mm, the corresponding normalized thickness and correction factor are $\Lambda_t = 32$ and $\chi_t = 0.752$, respectively. Therefore, the through-thickness reference strength in the proposed model is $\sigma_3^y = \chi_t \sigma_0$, corresponding to a 24.8% reduction of the through-thickness reference resistance relative to the bulk state.

Two simulations are performed under identical geometry, explosive loading, numerical discretization, equation of state, strain-hardening, strain-rate, and thermal-softening conditions. The first employs the isotropic J2 model defined by the bulk reference state

in Section 4.2, whereas the second employs the microstructural-length-scale-dependent formulation developed in Section 2. Thus, the controlled difference between the two calculations is the additional modification of the through-thickness plastic resistance associated with the finite microstructural length scale.

Three representative times are selected to characterize the principal stages of liner collapse, jet initiation, and jet stretching, denoted by $t_1 = 50$ μs, $t_2 = 80$ μs, and $t_3 = 90$ μs, respectively. Figure 9 compares the velocity and temperature fields predicted by the two constitutive models at these times. Both models reproduce the same overall sequence of detonation loading, liner acceleration, axial collapse, jet–slug formation, and subsequent jet elongation. During the early collapse stage, the two solutions exhibit similar global responses. As the collapse proceeds, differences develop in the local velocity and temperature fields, particularly in the main jet region. At t_3, the proposed model predicts higher local velocity and a redistributed temperature field in the main jet. The associated deformation and energy partitioning are examined quantitatively below through comparisons of temperature rise, equivalent plastic strain, specific plastic work, and specific kinetic energy.

To quantify the differences observed in Figure 9, the jet-tip velocity v_{tip} and jet length L_j are extracted at the same three representative times. The instantaneous jet length is defined as

$$L_j(t) = z_{\mathrm{tip}}(t) - z_{\mathrm{tail}}(t), \tag{85}$$

where z_{tip} and z_{tail} denote the axial positions of the jet head and the rear boundary of the continuously formed jet, respectively. The corresponding results are summarized in Table 7. The relative differences are evaluated using the J2 solution as the reference.

Table 7. Quantitative comparison of jet kinematics at the representative times used in Figure 9.

Time (μs)	v_{tip} (m/s)			L_j (mm)		
	J2	Proposed	Difference (%)	J2	Proposed	Difference (%)
50	5200	5600	7.69	75.97	81.53	7.32
80	4800	5300	10.42	232.02	244.35	5.31
90	4700	5300	12.77	319.35	334.36	4.70

The quantitative comparison shows that the difference in jet-tip velocity becomes increasingly pronounced as jet formation proceeds, whereas the relative difference in jet length remains moderate. At t_3, the proposed model predicts a jet-tip velocity of 5300 m/s, compared with 4700 m/s for the J2 model, corresponding to a difference of 12.77%. The corresponding jet lengths are 334.36 and 319.35 mm, respectively, indicating stronger axial stretching when the length-scale correction is included.

To further examine the internal kinematics of the formed jet, the axial velocity distribution is extracted at the third representative time t_3, when a continuous and substantially elongated jet has developed. To facilitate comparison between jets of different instantaneous lengths, the axial coordinate is normalized as

$$\bar{\xi} = \frac{z - z_{\mathrm{tail}}}{L_j}, \tag{86}$$

where $\bar{\xi} = 0$ and 1 correspond to the jet tail and jet tip, respectively. Figure 10 compares the resulting axial velocity profiles. Both simulations exhibit the characteristic increase in axial velocity from the rear portion toward the jet head. The proposed model predicts a larger head-to-rear axial velocity difference and a more pronounced velocity variation along the normalized jet coordinate. The head-to-rear velocity difference changes from 2139 m/s for the J2 model to 2416 m/s for the proposed model, consistent with the corresponding difference in jet elongation reported in Table 7.

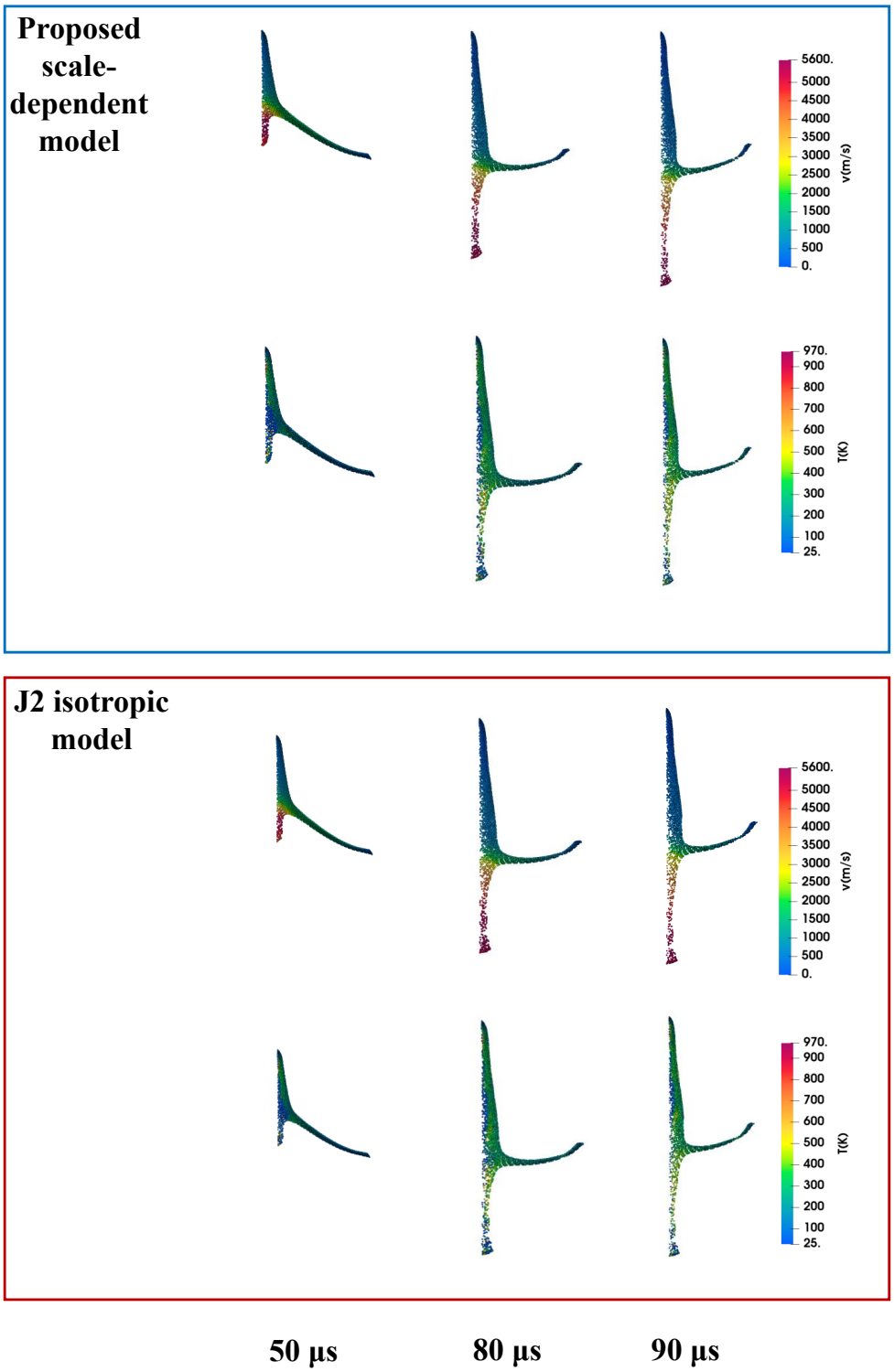


Figure 9. Comparison of the velocity and temperature fields predicted by the isotropic J2 and microstructural-length-scale-dependent models at three representative stages of liner collapse and jet formation.

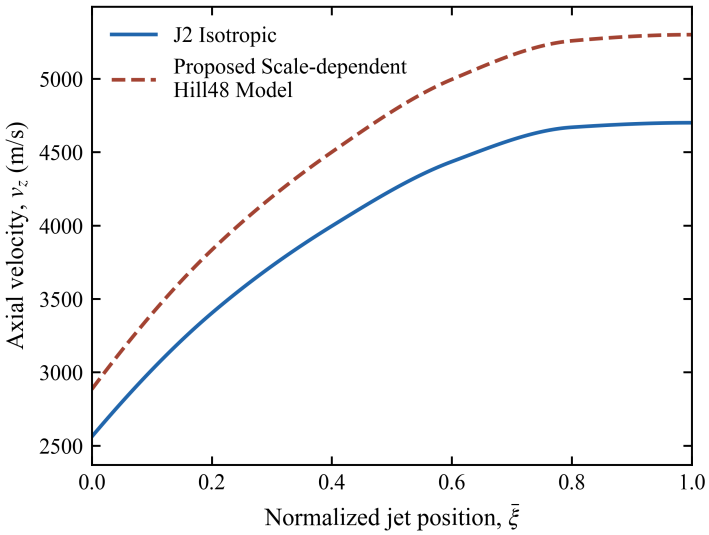


Figure 10. Axial velocity distributions along the continuously formed jet predicted by the isotropic J2 and microstructural-length-scale-dependent models at $t = 90$ μs.

The influence of the constitutive description on local deformation is further examined at the same representative time t_3. Figure 11 compares the equivalent plastic strain distributions and the locally enlarged jet-forming regions predicted by the two models. Severe plastic deformation is concentrated in the liner collapse and inversion region and subsequently extends into the stretching jet. The proposed model exhibits a higher equivalent plastic strain in the corresponding region than the J2 solution. More importantly, the enlarged views reveal a distinct difference in material continuity: the J2 model exhibits pronounced localized thinning and loss of local jet continuity, whereas the jet predicted by the proposed model remains continuous at the same instant. This difference indicates that the constitutive modification affects not only the magnitude of plastic deformation but also its spatial localization and the resulting local morphology of the forming jet. Overall, the microstructural-length-scale correction modifies local deformation and strain localization in the jet-forming region.

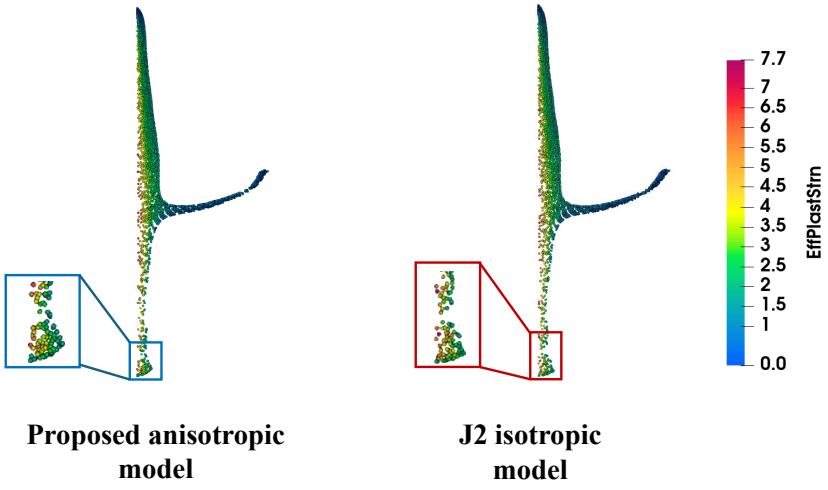


Figure 11. Comparison of the local deformation characteristics predicted by the isotropic J2 and microstructural-length-scale-dependent models at $t = 90$ μs.

The jet-tip and main-jet responses are compared at $t = 90$ μs to quantify the thermomechanical differences between the models. The main jet is defined as the continuous segment

ahead of the slug, spanning $z_{\mathrm{tail}} \le z \le z_{\mathrm{tip}}$. Main-jet quantities are averaged over all liner material within this region, using the same extraction procedure for both models.

As shown in Table 8, the proposed model increases the jet-tip velocity and main-jet specific kinetic energy by 12.77% and 8.01%, respectively, relative to J2. The jet-tip-region temperature rise and equivalent plastic strain increase by 2.92% and 4.82%. For the main jet, the average temperature rise, equivalent plastic strain, and specific plastic work increase by 3.58%, 3.61%, and 20.75%, respectively.

Table 8. Quantitative thermomechanical comparison between the J2 and proposed models at $t = 90$ μs for $D = 300$ mm and $t_0 = 8$ mm.

Quantity	J2	Proposed	Difference (%)
Jet-tip velocity, v_{tip} (m/s)	4700	5300	12.77
Jet-tip-region temperature rise, ΔT_{tip} (K)	259.95	267.53	2.92
Jet-tip-region equivalent plastic strain, $\bar{\varepsilon}^{p}_{\mathrm{tip}}$	2.49	2.61	4.82
Main-jet average temperature rise, $\langle \Delta T \rangle_{\mathrm{j}}$ (K)	271.24	280.94	3.58
Main-jet average equivalent plastic strain, $\langle \bar{\varepsilon}^{p} \rangle_{\mathrm{j}}$	1.66	1.72	3.61
Main-jet specific plastic work, w^{p}_{j} (MJ/kg)	0.53	0.64	20.75
Main-jet specific kinetic energy, e^{k}_{j} (MJ/kg)	7.37	7.96	8.01

Note: The relative difference is calculated with the J2 result as the reference.

The velocity and kinetic-energy increases characterize enhanced jet motion, while the temperature, strain, and plastic-work increases reflect changes in accumulated deformation and energy partitioning. Because the through-thickness plastic resistance is the controlled difference between the simulations, these concurrent changes provide quantitative support for the proposed mechanism within the present numerical framework.

Overall, under identical explosive loading and conventional thermoviscoplastic parameters, the proposed model predicts a higher jet-tip velocity and stronger axial stretching than the J2 reference in this representative case. Since the correction depends on the normalized thickness Λ_t, its variation with liner thickness and charge caliber is examined in the following subsection.

4.4. Liner-Thickness Effect and Multi-Caliber Critical-Thickness Relation

To further investigate the influence of liner thickness on jet formation, a series of simulations are performed for three representative large-caliber shaped charges with diameters of $D_1 = 250$ mm, $D_2 = 300$ mm, and $D_3 = 350$ mm. For each caliber, the initial liner thickness is varied around the transition from continuous to unstable jet formation. In the cases considered here, increasing the liner thickness eventually promotes local necking and plastic instability of the formed jet. Accordingly, the critical liner thickness t_c is defined as the upper thickness boundary for maintaining a continuous and noncritical jet during the prescribed early free-flight stage.

4.4.1. Jet-Stability Criterion Based on Plastic Instability

The jet stability is evaluated during an early free-flight stage rather than at the final breakup state, because a strongly stretched metallic jet may reach a critical plastic-instability condition before complete geometric separation occurs [65–69]. To compare different charge calibers at a consistent stage of jet development, the evaluation interval of the normalized free-flight distance is prescribed as

$$0.5 \le \bar{S}_f \le 0.75, \tag{87}$$

where the normalized free-flight distance is defined by

$$\bar{S}_f = \frac{S_f}{D} = \frac{z_{\mathrm{tip}} - z_b}{D}, \tag{88}$$

where z_{tip} is the instantaneous axial position of the jet tip, z_b is the initial axial position of the liner base, and D is the charge caliber. The lower bound ensures that a sufficiently elongated jet has formed, whereas the upper bound avoids later-stage breakup and large-amplitude geometric disturbances. This interval is used only as a common early free-flight comparison window and does not represent the final breakup distance or the optimum penetration standoff.

Following the Walsh-type plastic-instability description [66], the local instability parameter is written as

$$\phi(z,t) = \frac{\bar{\sigma}_H(z,t)}{\rho_j(z,t)\left[\partial v_z(z,t)/\partial z\right]^2 r_j^2(z,t)}, \tag{89}$$

where ρ_j, v_z, and r_j denote the current jet density, axial velocity, and local jet radius, respectively. The critical condition is defined by

$$\phi = \phi_c, \tag{90}$$

which gives the corresponding critical jet radius

$$r_{\mathrm{cr}}(z,t) = \frac{1}{|\partial v_z/\partial z|}\sqrt{\frac{\bar{\sigma}_H(z,t)}{\rho_j(z,t)\phi_c}}. \tag{91}$$

A dimensionless instability index is therefore introduced as

$$I_r(z,t) = \frac{r_j(z,t)}{r_{\mathrm{cr}}(z,t)}. \tag{92}$$

Accordingly, $I_r > 1$ indicates that the local jet radius remains above the critical value, whereas $I_r \leq 1$ indicates that the corresponding jet segment has reached the critical plastic-instability condition.

Because instability may first develop locally, the minimum index over the main continuous jet segment is defined as

$$I_{\min}(t) = \min_{z\in\Omega_j^*} I_r(z,t). \tag{93}$$

Using the normalized jet coordinate $\bar{\xi}$ defined in Equation (86), the evaluation domain is taken as

$$\Omega_j^* = \left\{z \,\middle|\, 0.05 \leq \bar{\xi} \leq 0.95\right\}, \tag{94}$$

thereby excluding the foremost and rearmost 5% of the instantaneous jet length, where the geometric tip and jet–slug transition may produce nonrepresentative local extrema. A case is classified as continuous and noncritical when

$$I_{\min}(t) > 1 \qquad \text{for} \qquad 0.5 \leq \bar{S}_f \leq 0.75, \tag{95}$$

with no complete material separation. If $I_{\min} \leq 1$ at any instant within this interval, the jet is regarded as having reached the critical plastic-instability condition.

All quantities required by the criterion are evaluated directly from the instantaneous HOTM solution. The local jet radius and density are obtained from the current material configuration, the Hill equivalent stress is evaluated from the constitutive state, and the axial velocity gradient is calculated directly from the derivatives of the LME interpolation functions rather than by finite-difference reconstruction. The instability threshold is treated as an effective breakup-related parameter. Following the Walsh-type framework

and representative results reported for copper shaped-charge jets [66,69,70], the present calculations adopt

$$\phi_c = 650. \tag{96}$$

This value is used as an effective parameter for the present numerical study and should not be interpreted as a universal material constant.

Figure 12 compares the evolution of $I_{\min}$ for the two liner thicknesses immediately bracketing the stable–unstable transition for each caliber. The thinner case t_s, defined as the largest stable thickness, maintains $I_{\min} > 1$ throughout the prescribed interval, whereas the slightly thicker case t_u, corresponding to the smallest unstable thickness, reaches or falls below the critical value $I_{\min} = 1$. Because the local jet radius, velocity gradient, density, and material resistance evolve simultaneously, moderate fluctuations in $I_{\min}$ may occur; the classification is therefore based on whether the critical value is reached within the prescribed interval rather than on monotonicity.

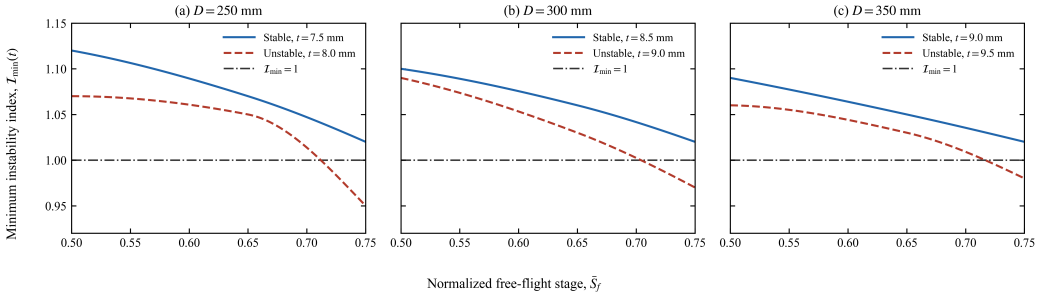


Figure 12. Evolution of the minimum instability index $\mathcal{J}_{\min}$ over the normalized early free-flight interval for the two liner thicknesses bracketing the stable–unstable transition. For each caliber, t_s denotes the largest stable thickness and t_u the smallest unstable thickness. The horizontal line $\mathcal{J}_{\min} = 1$ denotes the critical plastic-instability condition.

4.4.2. Critical Liner Thickness and Its Dependence on Charge Caliber

Using the instability criterion defined above, liner-thickness sweeps are performed for the three selected charge calibers. For each caliber, two adjacent cases are identified around the stable–unstable transition: the largest continuous and noncritical thickness t_s and the smallest unstable thickness t_u, with $t_s < t_u$. The critical liner thickness is therefore bracketed by

$$t_s < t_c \leq t_u. \tag{97}$$

Because the stable–unstable transition is identified from a discrete thickness sweep, the bracket in Equation (97) is taken as the primary result. The thickness-search resolution, nominal midpoint estimate, and bracket half-width are defined, respectively, as

$$\delta t_{\text{res}} = t_u - t_s, \tag{98}$$

$$\hat{t}_c = \frac{t_s + t_u}{2}, \tag{99}$$

$$\varepsilon_{\text{res}} = \frac{t_u - t_s}{2}. \tag{100}$$

The midpoint is used only for comparison among charge calibers. The bracket half-width characterizes the discrete search resolution and does not represent a statistical confidence interval or the total predictive uncertainty.

Table 9 summarizes the transition brackets and nominal estimates. For D = 250, 300, and 350 mm, the nominal critical thicknesses are 7.75, 8.75, and 9.25 mm, respectively, with a common thickness-search resolution of 0.5 mm.

As shown in Figure 13, $\hat{t}_c$ increases with charge caliber, whereas $\hat{t}_c/D$ decreases from 0.0310 to 0.0264, indicating a departure from strict geometric proportionality within

D = 250–350 mm. These three-caliber results represent a numerical trend rather than a general scaling law; additional calculations are needed to assess whether it persists over a broader range. The error bars in Figure 13a represent the transition-bracket half-width $\varepsilon_{\mathrm{res}}$, rather than statistical uncertainty.

The calculated trend reflects the combined influence of thickness-dependent constitutive response and caliber-dependent jet-forming dynamics. As the liner thickness increases relative to the effective microstructural characteristic length, the scale-dependent modification of the through-thickness plastic resistance gradually changes, while variations in inertia, deformation time scale, strain-rate evolution, thermal response, and detonation loading may also affect jet stretching and the onset of local instability. The transition brackets quantify only the thickness-search resolution and do not include uncertainties associated with constitutive parameters, numerical discretization, or the adopted instability threshold. The predictions should therefore not be interpreted as validated engineering design limits.

Table 9. Critical-thickness transition brackets and nominal midpoint estimates.

D (mm)	$t_s < t_c \leq t_u$ (mm)	δt_{res} (mm)	$\hat{t}_c$ (mm)	$\hat{t}_c/D$
250	$7.5 < t_c \leq 8.0$	0.5	7.75	0.0310
300	$8.5 < t_c \leq 9.0$	0.5	8.75	0.0292
350	$9.0 < t_c \leq 9.5$	0.5	9.25	0.0264

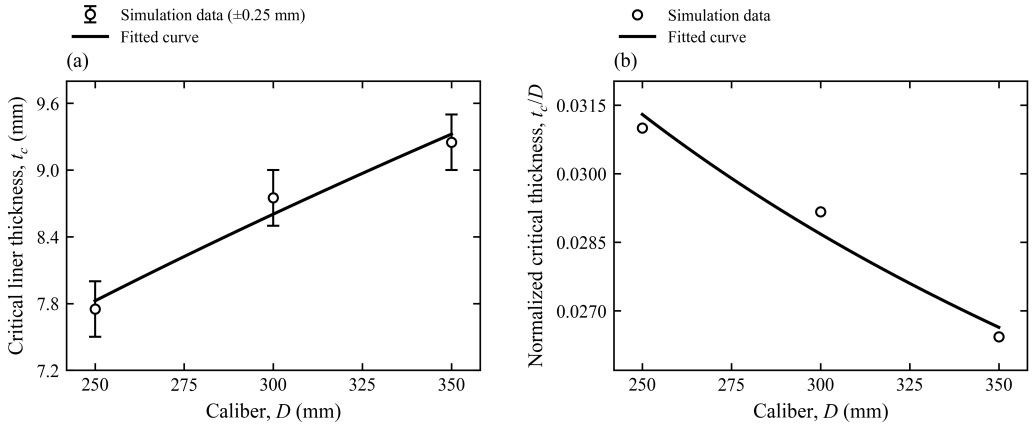


Figure 13. Dependence of the nominal critical-thickness estimate (**a**) and its normalized value (**b**) on charge caliber. The error bars in (**a**) represent the half-width of the numerical transition bracket, $\varepsilon_{\mathrm{res}} = (t_u - t_s)/2$, rather than a statistical uncertainty.

4.4.3. Sensitivity to the Instability Threshold

The instability threshold was varied by ±20% around $\phi_c = 650$, giving 520, 650, and 780. Because ϕ_c enters only the post-processing criterion, the existing simulation results were re-evaluated using

$$I_{\min}(t;\phi_c) = I_{\min}(t;650)\sqrt{\frac{\phi_c}{650}}. \tag{101}$$

These variations decrease and increase the instability index by approximately 10.6% and 9.5%, respectively.

For D = 250, 300, and 350 mm, the baseline stable boundary cases have liner thicknesses of 7.5, 8.5, and 9.0 mm, respectively, with a smaller endpoint index of 1.02 in each case. Reducing ϕ_c to 520 lowers this index to 0.912, reclassifying all three cases as unstable. The baseline unstable boundary cases have thicknesses of 8.0, 9.0, and 9.5 mm, with controlling indices of 0.95, 0.97, and 0.98, respectively. Increasing ϕ_c to 780 raises these indices to 1.041,

1.063, and 1.074, reclassifying the cases as stable. The resulting critical-thickness intervals are summarized in Table 10.

Table 10. Sensitivity of the predicted critical liner-thickness intervals to the instability threshold.

ϕ_c	$D = 250$ mm Critical Thickness (mm)	$D = 300$ mm Critical Thickness (mm)	$D = 350$ mm Critical Thickness (mm)
520	$7.0 < t_c \leq 7.5$	$8.0 < t_c \leq 8.5$	$8.5 < t_c \leq 9.0$
650	$7.5 < t_c \leq 8.0$	$8.5 < t_c \leq 9.0$	$9.0 < t_c \leq 9.5$
780	$8.0 < t_c \leq 8.5$	$9.0 < t_c \leq 9.5$	$9.5 < t_c \leq 10.0$

Decreasing or increasing ϕ_c shifts the critical-thickness intervals by 0.5 mm toward smaller or larger thicknesses, respectively. Although the absolute predictions are threshold dependent, the critical thickness increases with charge caliber for all three threshold values, preserving the caliber-dependent trend within the investigated range.

4.5. Mechanism Discussion and Model Limitations

Within the proposed constitutive framework, the length-scale correction modifies the through-thickness plastic resistance during liner acceleration, inversion, and convergence toward the symmetry axis. This change alters the local collapse kinematics and subsequently affects material partitioning, axial velocity distribution, jet stretching, and the development of localized thinning and necking. The stable–unstable transition identified in Section 4.4 also involves thickness-dependent changes in inertia, deformation history, and participating material mass, and therefore reflects both the constitutive correction and overall jet-forming dynamics. The concurrent changes in main-jet kinetic energy, plastic work, temperature rise, and accumulated plastic strain reported in Table 8 provide quantitative support for this mechanism-based interpretation.

Several modeling assumptions should be considered when interpreting these results. Although the Hill48 formulation permits independently specified bulk anisotropy, the present simulations adopt an isotropic bulk reference because reliable direction-dependent data for the considered liner are unavailable. This choice isolates the thickness-dependent directional contribution, but does not represent the complete manufacturing-induced anisotropy of an actual liner. The scale-dependent correction is restricted to the through-thickness normal resistance because of the relatively small thickness and finite number of grain layers or effective microstructural units in this direction. Possible scale dependence of the meridional, circumferential, and shear responses is neglected as a first-order approximation.

The characteristic length ℓ_t should therefore be interpreted as an effective microstructural scale rather than as a directly measured mean grain size. The parameters ℓ_t, A_t, Λ_0, and p have not been independently calibrated from thickness-dependent directional tests. Moreover, the combined scale $\ell_t\Lambda_0$ limits the independent identification of ℓ_t and Λ_0 without additional microstructural information. Consequently, the quantitative magnitude of the predicted thickness effect remains parameter dependent. The axisymmetric formulation captures rotationally symmetric collapse and early jet stretching, but cannot represent non-axisymmetric localization, asymmetric necking, or fully three-dimensional fragmentation.

The predicted critical-thickness transition is also criterion dependent. The Walsh-type threshold ϕ_c is literature informed rather than calibrated against breakup experiments for the specific liner, and its variation may shift the stable–unstable transition. With only three charge calibers examined, the increase in nominal critical thickness and decrease in its normalized value indicate a numerical trend within the investigated range, rather than a universal scaling law. The reported transition brackets quantify the finite resolution of the thickness sweep and should not be interpreted as the total predictive uncertainty.

The present calculations constitute a controlled numerical investigation of the effects of a finite-thickness microstructural scale, rather than independent validation of the adopted OFHC-copper parameterization. The principal contribution is a continuum framework linking liner thickness to an effective microstructural scale for systematic assessment of jet formation and stability. Dedicated material characterization and time-resolved shaped-charge experiments remain necessary for quantitative calibration and physical validation.

5. Conclusions

A Hill48-based thermoviscoplastic formulation incorporating an effective through-thickness microstructural length was developed and implemented in the axisymmetric HOTM framework. Directional-yield and material-coordinate transformation tests verified the constitutive implementation. The model recovers the prescribed bulk response as the scale effect vanishes. An isotropic bulk reference was adopted in the shaped-charge simulations to isolate the thickness-dependent directional correction.

For $D = 300$ mm and $t_0 = 8$ mm, the proposed model predicts a jet-tip velocity of 5300 m/s and a jet length of 334.36 mm at $t = 90$ μs, compared with 4700 m/s and 319.35 mm for the J2 reference. Differences in axial velocity distribution, deformation localization, and local jet continuity further demonstrate the influence of the thickness-dependent resistance within this controlled numerical comparison.

Using the Walsh-type instability criterion, the critical-thickness transitions were bracketed as 7.5–8.0, 8.5–9.0, and 9.0–9.5 mm for charge calibers of 250, 300, and 350 mm, respectively, with nominal midpoint estimates of 7.75, 8.75, and 9.25 mm. The corresponding decrease in $\hat{t}_c/D$ from 0.0310 to 0.0264 indicates a departure from strict geometric proportionality. This finding represents a numerical trend over the three investigated calibers, rather than a general scaling law. The transition brackets reflect the thickness-search resolution, not the total predictive uncertainty.

The principal contribution is a continuum framework linking liner thickness to an effective microstructural scale for assessing jet formation and stability. The predictions remain conditional on the adopted parameterization and do not constitute validated engineering design limits or a uniquely validated description of OFHC-copper behavior. Further material characterization, additional caliber calculations, and time-resolved shaped-charge experiments are required for quantitative calibration and physical validation.

Author Contributions: Conceptualization, W.Y. (Wanqian Yu) and H.W.; methodology, W.Y. (Wanqian Yu), Q.M., H.W. and B.L.; software, W.Y. (Wanqian Yu), Q.M., W.Y. (Wenhao Yue) and Z.H.; validation, W.Y. (Wanqian Yu), Q.M., S.Z., L.J., H.Z., Z.H. and Y.Y.; formal analysis, W.Y. (Wanqian Yu), W.Y. (Wenhao Yue) and H.W.; investigation, W.Y. (Wanqian Yu), Q.M. and H.W.; resources, W.Y. (Wanqian Yu), S.J. and B.L.; data curation, W.Y. (Wanqian Yu) and H.W.; writing—original draft preparation, W.Y. (Wanqian Yu) and Q.M.; writing—review and editing, S.Z., L.J., H.Z., H.W., S.J. and B.L.; visualization, Q.M., Z.H., H.L., and Y.Y.; supervision, L.J., S.J. and B.L.; project administration, L.J., S.J. and B.L.; funding acquisition, W.Y. (Wanqian Yu), H.W. and B.L. All authors have read and agreed to the published version of the manuscript.

Funding: This research is supported by the National Key Laboratory of Land and Air Based Information Perception and Control, China (Grant No.B424010), the Science and Technology Innovation Key R&D Program of Chongqing (Grant No. CSTB2025TIAD-STX0038), the Key R&D Program of Jiangxi Province, China (Grant No. 20252BCG330006), and the National Natural Science Foundation of China (Grant No. 12372205).

Data Availability Statement: Data will be made available on request.

Conflicts of Interest: Authors Wenhao Yue, Hao Wang, Zhida Huang, Huming Liao, and Yanhong Yang are employed by the company Xi'an Zhonglang Intelligent Control Technology Co., Ltd. and

ESCAAS Co., Ltd. The remaining authors declare that the research was conducted in the absence of any commercial or financial relationships that could be construed as a potential conflict of interest.

Nomenclature

1. Axisymmetric Kinematics and Material Coordinates

1.1 Reference and current coordinates

θ	Circumferential coordinate/direction in the cylindrical system	rad
R, Z	Radial and axial material coordinates in the reference configuration	m
r, z	Radial and axial coordinates in the current configuration	m
$\mathbf{X}(R, Z)$, $\mathbf{x}(r, z)$	Material-point position vectors in the reference and current configurations	m

1.2 Cylindrical and local material bases

$\mathbf{e}_r, \mathbf{e}_\theta, \mathbf{e}_z$	Cylindrical radial, circumferential, and axial basis vectors	–
$\mathbf{a}_1, \mathbf{a}_2, \mathbf{a}_3$	Local orthonormal material basis in the meridional, circumferential, and through-thickness directions	–
α	Angle between the local meridional direction $\mathbf{a}_1$ and the radial direction	rad or °

1.3 Deformation kinematics

u_θ	Circumferential velocity component	$\mathrm{m\,s^{-1}}$
$\boldsymbol{\varphi}$	Deformation mapping	m
$\hat{\nabla}_0$	Gradient operator with respect to the reference configuration	$\mathrm{m^{-1}}$
$\mathbf{F}$	Deformation gradient tensor	–
$\mathbf{F}^e, \mathbf{F}^p$	Elastic and plastic deformation-gradient tensors	–
J	Determinant of the deformation gradient, $\det \mathbf{F}$	–

1.4 Coordinate and tensor transformations

$\mathbf{Q}_c$	Transformation matrix from the local material basis to the cylindrical basis	–
$\boldsymbol{\sigma}, \boldsymbol{\sigma}^m$	Stress tensor in the cylindrical and local material coordinate systems	Pa
σ_{ij}^m	Components of the stress tensor in the local material coordinate system	Pa

2. Constitutive Material Models

2.1 Thermodynamic state and free energy

T	Temperature	K
T_0	Reference (initial) temperature	K
$\mathbf{Z}$	Vector/set of internal state variables	Various
A	Helmholtz free-energy density	$\mathrm{J\,m^{-3}}$
$W^{e,\mathrm{vol}}$, $W^{e,\mathrm{dev}}$, W^p, W^h	Volumetric elastic, deviatoric elastic, plastic-storage, and thermal free-energy contributions	$\mathrm{J\,m^{-3}}$
$C(T)$	Temperature-dependent specific heat capacity per unit reference volume	$\mathrm{J\,m^{-3}\,K^{-1}}$
$\mathbf{G}$	Thermal driving vector, $-T^{-1}\nabla_0 T$	$\mathrm{m^{-1}}$

2.2 Mie–Grüneisen volumetric response

p	Pressure	Pa
ρ_0, ρ	Reference and current mass densities	$\mathrm{kg\,m^{-3}}$
μ	Compression measure, $\rho/\rho_0 - 1$	–
C_0	Reference bulk sound speed	$\mathrm{m\,s^{-1}}$
c_0	Bulk sound speed listed for the explosive and liner	$\mathrm{m\,s^{-1}}$
E	Internal energy per unit reference volume	$\mathrm{J\,m^{-3}}$
S_1, S_2, S_3	Shock-velocity–particle-velocity relation coefficients	–
s	Hugoniot slope coefficient of the unreacted explosive	–
γ_0	Grüneisen parameter in the generic Mie–Grüneisen EOS	–
Γ_s	Grüneisen coefficient of the unreacted solid explosive	–
b	Second Grüneisen parameter in the generic Mie–Grüneisen EOS	–

2.3 Elastic and thermophysical response of the liner		
$G(T)$	Temperature-dependent shear modulus	Pa
G_t	Reference shear modulus	Pa
G_0	Initial shear modulus	Pa
a	Temperature-sensitivity coefficient	K^{-1}
T_c	Reference temperature	K
$\mathbf{e}^{e,\mathrm{dev}}$	Deviatoric elastic logarithmic strain tensor	–
ν	Poisson's ratio of the liner	–
c_p	Mass-specific heat capacity	$J\,kg^{-1}\,K^{-1}$
2.4 Hill48 anisotropic yield model		
Φ	Hill48 quadratic stress form	Pa^2
$\bar{\sigma}_H$	Hill48 equivalent stress	Pa
$F_H, G_H, H_H, L_H, M_H, N_H$	Dimensionless Hill48 anisotropy coefficients	–
$\sigma_1^y, \sigma_2^y, \sigma_3^y$	Reference normal yield strengths in the meridional, circumferential, and through-thickness directions	Pa
τ_{31}^y	Reference shear yield strength in the local 3–1 plane	Pa
σ_{ref}	Fixed reference stress used to normalize directional yield strengths	Pa
f	Yield function	Pa
2.5 Thermoviscoplastic flow and hardening		
σ_y	Current thermoviscoplastic flow stress	Pa
σ_0	Initial yield stress at the reference state	Pa
$\bar{\varepsilon}^p$, $\dot{\bar{\varepsilon}}^p$	Accumulated equivalent plastic strain and equivalent plastic strain rate	–, s^{-1}
$\bar{\varepsilon}_0^p$, $\dot{\bar{\varepsilon}}_0^p$	Reference equivalent plastic strain and reference equivalent plastic strain rate	–, s^{-1}
n	Strain-hardening parameter	–
m	Rate-sensitivity parameter	–
l	Thermal-softening exponent	–
T_m	Melting temperature	K
$\dot{\lambda}$	Non-negative plastic multiplier	s^{-1}
$\mathbf{D}^{p,m}$	Plastic rate-of-deformation tensor in local material coordinates	s^{-1}
$\mathbf{H}^m$	Gradient of Hill equivalent stress with respect to local stress	–
2.6 Plastic dissipation and temperature rise		
β	Taylor–Quinney coefficient (fraction of plastic work converted into heat)	–
β_{TQ}	Taylor–Quinney coefficient	–
$\dot{T}_p$	Temperature-rise rate caused by plastic dissipation	$K\,s^{-1}$
2.7 Microstructural length-scale correction		
ℓ_t	Effective through-thickness microstructural characteristic length	mm
Λ_t	Normalized liner thickness, t_0/ℓ_t	–
$\chi_t(\Lambda_t)$	Through-thickness strength correction factor	–
A_t	Maximum strength-reduction amplitude	–
Λ_0	Characteristic normalized transition scale	–
p	Transition exponent in the microstructural correction law	–
$\sigma_{3,\infty}^y$	Bulk-limit through-thickness reference yield strength	Pa
2.8 Arrhenius thermal reaction		
λ	Explosive reaction-progress variable	–
A_A	Arrhenius pre-exponential factor	s^{-1}
E_a	Activation energy	$J\,mol^{-1}$
R	Universal gas constant	$J\,mol^{-1}\,K^{-1}$
2.9 Ignition-and-Growth reaction		
R_I, R_{G1}, R_{G2}	Ignition, first-growth, and second-growth reaction-rate terms	s^{-1}
I	Ignition coefficient	s^{-1}
a	Compression threshold in the ignition term	–

b	Unreacted-fraction exponent in the ignition term	–
x	Compression exponent in the ignition term	–
G_1, G_2	First- and second-growth coefficients	$\mathrm{Pa}^{-2}\,\mathrm{s}^{-1}$
c, d, y	Unreacted-fraction, reacted-fraction, and pressure exponents in the first-growth term	–
e, g, z	Unreacted-fraction, reacted-fraction, and pressure exponents in the second-growth term	–
$\lambda_{I,\max}, \lambda_{G1,\max}, \lambda_{G2,\min}$	Reaction-progress limits for ignition and growth terms	–
2.10 JWL product EOS and mixture response		
p_g	Pressure of gaseous reaction products	Pa
$A_{\mathrm{JWL}}, B_{\mathrm{JWL}}$	JWL pressure coefficients	Pa
R_1, R_2	JWL exponential coefficients	–
θ	Density ratio ρ/ρ_0 in the JWL equation of state	–
ω	JWL Grüneisen coefficient	–
E_0	Initial detonation-product energy density	$\mathrm{J\,m}^{-3}$
$\mathbf{I}$	Second-order identity tensor	–
$\boldsymbol{\sigma}_e, \boldsymbol{\sigma}_s$	Explosive-mixture stress tensor and unreacted-solid-phase stress tensor	Pa
3. HOTM Variational and Numerical Formulation		
3.1 Variational thermomechanics		
K	Kinetic-energy density	$\mathrm{J\,m}^{-3}$
η	Entropy density, $-\partial A/\partial T$	$\mathrm{J\,m}^{-3}\,\mathrm{K}^{-1}$
$\Omega_0, \Gamma_t, \Gamma_q$	Reference domain, traction boundary, and heat-flux boundary	–
$\mathbf{B}$	Body force per unit mass	$\mathrm{m\,s}^{-2}$
$\mathbf{T}$	Prescribed traction vector	Pa
$\bar{h}$	Prescribed boundary heat flux	$\mathrm{W\,m}^{-2}$
$\mathbf{q}$	Heat-flux vector	$\mathrm{W\,m}^{-2}$
3.2 Temporal discretization		
t_n, t_{n+1}	Beginning and end times of time step n	s
3.3 Meshfree spatial discretization		
w_p	Axisymmetric integration weight of material point p	m^3
r_p	Radial coordinate of material point p	m
s_p	Area represented by material point p in the meridional plane	m^2
N_a	Local maximum-entropy shape function associated with node a	–
m_a	Nodal mass	kg
$\boldsymbol{\varphi}^h, T^h$	Spatially approximated deformation/kinematic field and temperature field	m, K
$\boldsymbol{\varphi}_a, T_a$	Nodal kinematic variable and nodal temperature	m, K
3.4 Axisymmetric balance and near-axis treatment		
$P_{rr}, P_{rz}, P_{zz}, P_{\theta\theta}$	Stress components used in the axisymmetric internal-force equations	Pa
h	Characteristic nodal spacing	m
r_c	Near-axis activation radius	m
r_0	Near-axis regularization length	m
r_{eff}	Effective regularized radius	m
$\bar{r}$	Blended radius used to regularize singular geometric factors	m
$w(r)$	Near-axis radius-blending function	–
α	Near-axis activation-radius coefficient	–
η	Near-axis regularization coefficient	–
Ω_{axis}	Near-axis regularization region	–
u_r, v_r	Radial displacement and radial velocity components on the symmetry axis	m, $\mathrm{m\,s}^{-1}$
4. Constitutive Verification Parameters		
4.1 Directional-yield and transformation tests		
$\mathbf{n}$	Unit vector in the prescribed uniaxial loading direction	–
ψ	Loading angle measured from the local meridional material direction	°

β	Global loading-direction angle	$^\circ$
σ	Scalar uniaxial stress magnitude in the constitutive verification test	Pa
$C_H(\psi, \Lambda_t)$	Directional Hill48 coefficient for uniaxial loading	–
$\sigma^y_{\mathrm{dir}}(\psi, \Lambda_t)$	Analytical directional yield strength	Pa
5. Shaped-Charge Configuration and Simulation Outputs		
5.1 Geometry and case design		
D	Charge caliber (charge diameter)	mm
t_0	Initial liner thickness	mm
5.2 Numerical resolution		
$h_{\mathrm{mp}}^{\mathrm{liner}}$	Liner material-point spacing	mm
$h_{\mathrm{mp}}^{\mathrm{exp}}$	Explosive material-point spacing	mm
γ	LME locality parameter	–
5.3 Representative times and jet kinematics		
t_1, t_2, t_3	Representative times for collapse, jet initiation, and jet stretching	μs
v_{tip}	Jet-tip velocity	m s^{-1}
L_j	Instantaneous length of the continuously formed jet	mm
$z_{\mathrm{tip}}, z_{\mathrm{tail}}$	Axial positions of the jet head and rear boundary of the continuous jet	mm
$\bar{\xi}$	Normalized axial coordinate along the continuous jet	–
v_z	Axial jet velocity	m s^{-1}
6. Walsh-Type Plastic Instability and Critical Liner Thickness		
6.1 Free-flight evaluation window		
S_f	Jet-tip free-flight distance measured from the initial liner-base position	mm
$\bar{S}_f$	Normalized jet-tip free-flight distance, S_f/D	–
z_b	Initial axial position of the liner base	mm
6.2 Local plastic-instability criterion		
$\varphi(z,t)$	Local Walsh-type plastic-instability parameter	–
φ_c	Critical instability threshold	–
$\rho_j(z,t)$	Current local jet density	kg m^{-3}
$r_j(z,t)$	Local current jet radius	mm
$r_{\mathrm{cr}}(z,t)$	Critical local jet radius	mm
$I_r(z,t)$	Dimensionless local instability index	–
$I_{\min}(t)$	Minimum local instability index over the main continuous jet segment	–
Ω_j^*	Evaluation domain over the central 90 percent of the instantaneous jet length	–
6.3 Critical-thickness bracket and estimate		
t_s, t_u	Largest stable thickness and smallest unstable thickness	mm
t_c	Critical liner thickness	mm
$\hat{t}_c$	Nominal midpoint estimate of the critical liner thickness	mm
δt_{res}	Thickness-search resolution	mm
$\varepsilon_{\mathrm{res}}$	Half-width of the critical-thickness transition bracket	mm
7. Common Notation and Abbreviations		
7.1 Common time variable, indices, and affixes		
t	Time	s
$1, 2, 3$	Local meridional, circumferential, and through-thickness material directions	–
r, θ, z	Radial, circumferential, and axial cylindrical component labels	–
m	Superscript indicating quantities expressed in the local material coordinate system	–
e, p	Elastic and plastic superscripts	–
vol, dev, h	Volumetric, deviatoric, and thermal free-energy labels	–
0, ref, ∞	Initial/reference state, fixed reference quantity, and bulk-limit value	–
a	Node index	–

p	Material-point index	–
$n, n+1$	Current and next time-step indices	–
int, ext	Internal and external nodal contributions	–
T, p	Temperature-driven and pressure-driven reaction-rate labels	–
7.2 Abbreviations and model names		
HOTM	Hot Optimal Transportation Meshfree	–
EOS	Equation of state	–
Hill48	Hill's 1948 anisotropic quadratic yield criterion	–
J2	Isotropic von Mises (second deviatoric invariant) plasticity model	–
LME	Local maximum entropy	–
EBSD	Electron backscatter diffraction	–
IG	Ignition and Growth	–
JWL	Jones–Wilkins–Lee	–
PBX	Polymer-bonded explosive	–
HMX	Cyclotetramethylene-tetranitramine explosive crystal	–
OFHC	Oxygen-free high-conductivity copper	–

References

1. Birkhoff, G.; MacDougall, D.P.; Pugh, E.M.; Taylor, G.I. Explosives with Lined Cavities. *J. Appl. Phys.* **1948**, *19*, 563–582. [CrossRef]
2. Pugh, E.M.; Eichelberger, R.J.; Rostoker, N. Theory of Jet Formation by Charges with Lined Conical Cavities. *J. Appl. Phys.* **1952**, *23*, 532–536. [CrossRef]
3. Eichelberger, R.J.; Pugh, E.M. Experimental Verification of the Theory of Jet Formation by Charges with Lined Conical Cavities. *J. Appl. Phys.* **1952**, *23*, 537–542. [CrossRef]
4. Yeom, G.S. Numerical Simulation of Conical and Linear-Shaped Charges Using an Eulerian Elasto-Plastic Multi-Material Multi-Phase Flow Model with Detonation. *Materials* **2022**, *15*, 1700. [CrossRef] [PubMed]
5. Song, P.; Li, W.; Liu, J.; Zhang, Q.; Wang, Z. Research on Plastic Flow Characteristic Parameter Distribution of Shaped-Charge Jet: Theory, Experiment, and Simulation. *Appl. Sci.* **2023**, *13*, 5128. [CrossRef]
6. Pyka, D.; Kurzawa, A.; Bocian, M.; Bajkowski, M.; Magier, M.; Śliwiński, J.; Jamroziak, K. Numerical and Experimental Studies of the ŁK Type Shaped Charge. *Appl. Sci.* **2020**, *10*, 6742. [CrossRef]
7. Ma, B.; Huang, Z.; Wu, Y.; Wang, Y.; Jia, X.; Gao, G. Research on the Formation Characteristics of the Shaped Charge Jet from the Shaped Charge with a Trapezoid Cross-Section. *Materials* **2022**, *15*, 8663. [CrossRef] [PubMed]
8. Cui, P.; Gao, X.; Xu, J.; Wen, J.; Cui, L.; Li, C.; Yang, Y. Simulation and Experimental Study on Jet Velocity of Zr-Based Amorphous Alloy Liner. *Metals* **2022**, *12*, 978. [CrossRef]
9. Zhang, X.; Xu, C.; Yi, J.; Li, X.; Yin, J. Analysis of Strength Effects on the Dynamic Response of a Shaped-Charge under Lateral Disturbances. *Appl. Sci.* **2025**, *15*, 6313. [CrossRef]
10. Zhang, Y.; Zhang, X.; Zhao, W.; Hu, F. Similarity Law Study of Shaped Charges Penetrating a Concrete Target. *Buildings* **2022**, *12*, 2268. [CrossRef]
11. Jiang, Y.; Gu, R.C.; Wang, J.T.; Xiao, Q.Q.; Huang, Z.X. Investigation on the Grain Size Effect on the Copper Shaped Charge Jet Stretching Behavior. *Front. Mater.* **2022**, *9*, 1017629. [CrossRef]
12. Agu, H.O.; Hameed, A.; Appleby-Thomas, G.J. Comparison of the Microstructure of Machined and Laser Sintered Shaped Charge Liner in the Hydrodynamic Regime. *J. Dyn. Behav. Mater.* **2019**, *5*, 484–494. [CrossRef]
13. Sun, S.; Jiang, J.; Wang, S.; Men, J.; Li, M.; Wang, Y. Comparison of Shaped Charge Jet Performance Generated by Machined and Additively Manufactured CuSn10 Liners. *Materials* **2021**, *14*, 7149. [CrossRef] [PubMed]
14. Meng, B.; Zhang, Y.Y.; Cheng, C.; Han, J.Q.; Wan, M. Effect of Plastic Anisotropy on Microscale Ductile Fracture and Microformability of Stainless Steel Foil. *Int. J. Mech. Sci.* **2018**, *148*, 620–635. [CrossRef]
15. Meng, B.; Wang, W.H.; Zhang, Y.Y.; Wan, M. Size Effect on Plastic Anisotropy in Microscale Deformation of Metal Foil. *J. Mater. Process. Technol.* **2019**, *271*, 46–61. [CrossRef]
16. Cheng, C.; Wan, M.; Meng, B.; Zhao, R.; Han, W.P. Size Effect on the Yield Behavior of Metal Foil under Multiaxial Stress States: Experimental Investigation and Modelling. *Int. J. Mech. Sci.* **2019**, *151*, 760–771. [CrossRef]
17. Yoshida, K. Effects of Grain-Scale Heterogeneity on Surface Roughness and Sheet Metal Necking. *Int. J. Mech. Sci.* **2014**, *83*, 48–56. [CrossRef]

18. Johnson, G.R.; Cook, W.H. A Constitutive Model and Data for Metals Subjected to Large Strains, High Strain Rates and High Temperatures. In *Proceedings of the 7th International Symposium on Ballistics, The Hague, The Netherlands, 1983*; American Defense Preparedness Association: Washington, DC, USA, 1983; pp. 541–547.
19. Steinberg, D.J.; Cochran, S.G.; Guinan, M.W. A Constitutive Model for Metals Applicable at High-Strain Rate. *J. Appl. Phys.* **1980**, *51*, 1498–1504. [CrossRef]
20. Zerilli, F.J.; Armstrong, R.W. Dislocation-Mechanics-Based Constitutive Relations for Material Dynamics Calculations. *J. Appl. Phys.* **1987**, *61*, 1816–1825. [CrossRef]
21. Follansbee, P.S.; Kocks, U.F. A Constitutive Description of the Deformation of Copper Based on the Use of the Mechanical Threshold Stress as an Internal State Variable. *Acta Metall.* **1988**, *36*, 81–93. [CrossRef]
22. Preston, D.L.; Tonks, D.L.; Wallace, D.C. Model of Plastic Deformation for Extreme Loading Conditions. *J. Appl. Phys.* **2003**, *93*, 211–220. [CrossRef]
23. Doney, R.L.; Niederhaus, J.H.J.; Fuller, T.J.; Coppinger, M.J. Effects of Equations of State and Constitutive Models on Simulating Copper Shaped Charge Jets in ALEGRA. *Int. J. Impact Eng.* **2020**, *136*, 103428. [CrossRef]
24. Hill, R. A Theory of the Yielding and Plastic Flow of Anisotropic Metals. *Proc. R. Soc. London. Ser. A Math. Phys. Sci.* **1948**, *193*, 281–297. [CrossRef]
25. Rassokha, S.S.; Ladov, S.V.; Kubyshkina, G.A.; Babkin, A.V. Performance Calculation of Shaped Charges with Shear-Formed Liners. *J. Appl. Mech.* **2013**, *80*, 031703. [CrossRef]
26. Schwartz, A.; Busche, M.; Becker, R.; Kumar, M.; Nikkel, D. Role of texture in spin formed Cu shaped-charge liners. In *Proceedings of the 19th International Symposium on Ballistics, Switzerland*; Technomic Publishing: Lancaster, PA, USA, 2001; pp. 733–740.
27. Becker, R.; Busche, M.; Schwartz, A.; Kumar, M. *Applications of Crystal Plasticity in Multiscale Modeling*; Technical Report; Lawrence Livermore National Lab.: Livermore, CA, USA, 2001.
28. Wang, Y.; Liu, J.; Liu, X.; Feng, X.; Du, Y.; Cao, J. Revealing the Influence of Material Properties of Shaped Charge Liner on Penetration Performance via Numerical Simulation and Machine Learning. *Materials* **2025**, *18*, 2742. [CrossRef] [PubMed]
29. Wang, H.; Liao, H.; Fan, Z.; Fan, J.; Stainier, L.; Li, X.; Li, B. The Hot Optimal Transportation Meshfree (HOTM) method for materials under extreme dynamic thermomechanical conditions. *Comput. Methods Appl. Mech. Eng.* **2020**, *364*, 112958. [CrossRef]
30. Wang, H. The Hot Optimal Transportation Meshfree (HOTM) Method for Extreme Multi-Physics Problems. Ph.D. Thesis, Case Western Reserve University, Cleveland, OH, USA, 2021.
31. Yu, W.; Ma, Q.; Zhao, S.; Ji, L.; Zhang, H.; Wang, H.; Huang, Z.; Liao, H.; Yang, Y.; Jin, S.; et al. An Axisymmetric Hot Optimal Transportation Meshfree Method with Near-Axis Stabilization for Shaped-Charge Jet Formation. *Comput. Part. Mech.* **2026**, *18*, 491–518. [CrossRef]
32. Lee, E.H. Elastic-plastic deformation at finite strains. *J. Appl. Mech.* **1969**, *36*, 1–6. [CrossRef]
33. Mie, G. Zur kinetischen Theorie der einatomigen Körper. *Ann. Phys.* **1903**, *316*, 657–697. [CrossRef]
34. Grüneisen, E. Theorie des festen Zustandes einatomiger Elemente. *Ann. Phys.* **1912**, *344*, 257–306. [CrossRef]
35. Segletes, S.B. Thermodynamic stability of the Mie–Grüneisen equation of state, and its relevance to hydrocode computations. *J. Appl. Phys.* **1991**, *70*, 2489–2499. [CrossRef]
36. Arienti, M.; Morano, E.; Shepherd, J. *Shock and Detonation Modeling with the Mie-Grüneisen Equation of State*; Graduate Aeronautical Laboratories Report FM99-8; California Institute of Technology: Pasadena, CA, USA, 2004.
37. Heuzé, O. General form of the Mie–Grüneisen equation of state. *Comptes Rendus. Méc.* **2012**, *340*, 679–687. [CrossRef]
38. Li, B.; Habbal, F.; Ortiz, M. Optimal transportation meshfree approximation schemes for fluid and plastic flows. *Int. J. Numer. Methods Eng.* **2010**, *83*, 1541–1579. [CrossRef]
39. Yang, Q.; Stainier, L.; Ortiz, M. A variational formulation of the coupled thermo-mechanical boundary-value problem for general dissipative solids. *J. Mech. Phys. Solids* **2006**, *54*, 401–424. [CrossRef]
40. Stainier, L.; Ortiz, M. Study and validation of a variational theory of thermo-mechanical coupling in finite visco-plasticity. *Int. J. Solids Struct.* **2010**, *47*, 705–715. [CrossRef]
41. Wang, H.; Li, B.; Fan, Z.; Li, X. Numerical modeling of the hot forming process of composite materials. In *Proceedings of the International Manufacturing Science and Engineering Conference*; American Society of Mechanical Engineers: New York, NY, USA, 2019; Volume 58752, p. V002T03A034.
42. Jiang, H.; Scott, V.; Li, B. Modeling and simulations of high and hypervelocity impact of small ice particles. *Int. J. Impact Eng.* **2021**, *155*, 103906. [CrossRef]
43. Jiang, H.; Wang, H.; Scott, V.; Li, B. Numerical analysis of oblique hypervelocity impact damage to space structural materials by ice particles in cryogenic environment. *Acta Astronaut.* **2022**, *195*, 392–404. [CrossRef]
44. Huang, Z.; Fan, Z.; Wang, H.; Li, B. Numerical Study of Grain Growth in Laser Powder Bed Fusion Additive Manufacturing of Metals. *Int. J. Comput. Methods* **2022**, *19*, 2141012. [CrossRef]
45. Wang, H.; Li, X.; Phipps, M.; Li, B. Numerical and experimental study of hot pressing technique for resin-based friction composites. *Compos. Part A Appl. Sci. Manuf.* **2022**, *153*, 106737. [CrossRef]

46. Wang, H.; Liao, H.; Wang, M.; Wang, X.; Fan, Z.; Li, B. Numerical approach for a strongly coupled thermomechanical process with multi-phase transition and applications in additive manufacturing. *Sci. Sin. Phys. Mech. Astron.* **2022**, *52*, 104713.
47. Huang, Z.; Wang, H.; Chen, L.; Gomez, H.; Li, B.; Cao, C. A meshfree phase-field model for simulating the sintering process of metallic particles for printed electronics. *Eng. Comput.* **2024**, *40*, 2241–2257. [CrossRef]
48. Wang, H.; Yang, H.; Navas, P.; Huang, Z.; Li, B. A thermomechanical multiphase meshfree solution for hot-pressing manufacturing of resin-based composites. *Comput. Part. Mech.* **2025**, *12*, 4205–4228. [CrossRef]
49. Arroyo, M.; Ortiz, M. Local maximum-entropy approximation schemes: A seamless bridge between finite elements and meshfree methods. *Int. J. Numer. Methods Eng.* **2006**, *65*, 2167–2202. [CrossRef]
50. Wang, C.; Ding, J.; Zhao, H. Numerical simulation on jet formation of shaped charge with different liner materials. *Def. Sci. J.* **2015**, *65*, 279–286. [CrossRef]
51. Yu, W.; Ma, Q.; Wang, H.; Ji, L.; Zhao, S.; Wang, C.; Yang, Y.; Yang, H.; Chen, J.; Guo, Z.; et al. Numerical study on the ignition/detonation mechanism of explosives and the associated structural failure under thermo-mechanical stimuli. *Comput. Part. Mech.* **2026**, *14*, 312–333. [CrossRef]
52. Berndt, P.; Klein, R. Modeling the kinetics of the Shockless Explosion Combustion. *Combust. Flame* **2017**, *175*, 16–26. [CrossRef]
53. Jensen, T.L.; Moxnes, J.F.; Unneberg, E.; Christensen, D. Models for predicting impact sensitivity of energetic materials based on the trigger linkage hypothesis and Arrhenius kinetics. *J. Mol. Model.* **2020**, *26*, 65. [CrossRef] [PubMed]
54. Lee, E.L.; Tarver, C.M. Phenomenological model of shock initiation in heterogeneous explosives. *Phys. Fluids* **1980**, *23*, 2362–2372. [CrossRef]
55. Awan, M.S.; Huang, Z.; Zu, X.; Xiao, Q.; Ma, B. Application of Lee–Tarver Model for Energetic Materials Safety Assessment Utilized in Aerospace Applications. *Aerospace* **2024**, *11*, 513. [CrossRef]
56. Lee, E.; Finger, M.; Collins, W. *JWL Equation of State Coefficients for High Explosives*; Technical Report; Lawrence Livermore National Lab.(LLNL): Livermore, CA, USA, 1973.
57. Baudin, G.; Serradeill, R. Review of Jones-Wilkins-Lee equation of state. In *Proceedings of the EPJ Web of Conferences*; EDP Sciences: Les Ulis, France, 2010; Volume 10, p. 00021.
58. Menikoff, R. *JWL Equation of State*; Technical Report; Los Alamos National Laboratory (LANL): Los Alamos, NM, USA, 2015.
59. Pedroso, D.M. A consistent u-p formulation for porous media with hysteresis. *Int. J. Numer. Methods Eng.* **2015**, *101*, 606–634. [CrossRef]
60. Tarver, C.; Forbes, J.; Garcia, F.; Urtiew, P. Manganin gauge and reactive flow modeling study of the shock initiation of PBX 9501. In *Proceedings of the AIP Conference Proceedings*; American Institute of Physics: Melville, NY, USA, 2002; Volume 620, pp. 1043–1046.
61. Menikoff, R. Detonation wave profile in PBX 9501. In *Proceedings of the AIP Conference Proceedings*; American Institute of Physicss: Melville, NY, USA, 2006; Volume 845, pp. 986–989.
62. Wei, Y.; Miller, C.; Olsen, D.; Zhou, M. Prediction of probabilistic shock initiation thresholds of energetic materials through evolution of thermal-mechanical dissipation and reactive heating. *J. Appl. Mech.* **2021**, *88*, 091005. [CrossRef]
63. Meyers, M.A. *Dynamic Behavior of Materials*; John Wiley & Sons: Hoboken, NJ, USA, 1994.
64. Vignjevic, R.; Campbell, J.C.; Bourne, N.K.; Djordjevic, N. Modeling shock waves in orthotropic elastic materials. *J. Appl. Phys.* **2008**, *104*, 044904. [CrossRef]
65. Chou, P.C.; Carleone, J. The stability of shaped-charge jets. *J. Appl. Phys.* **1977**, *48*, 4187–4195. [CrossRef]
66. Walsh, J. Plastic instability and particulation in stretching metal jets. *J. Appl. Phys.* **1984**, *56*, 1997–2006. [CrossRef]
67. Walters, W.P.; Summers, R.L. A review of jet breakup time models. *Propellants Explos. Pyrotech.* **1993**, *18*, 241–246. [CrossRef]
68. Petit, J.; Jeanclaude, V.; Fressengeas, C. Breakup of copper shaped-charge jets: Experiment, numerical simulations, and analytical modeling. *J. Appl. Phys.* **2005**, *98*, 123521. [CrossRef]
69. Miers, K.T.; Peterson, N.R.; Perry, W.L.; Lystrom, L.A.; Sweitzer, J.C.; DeFisher, S.E. Modeling and analysis of a 66 mm shaped charge. *Int. J. Impact Eng.* **2025**, *206*, 105396. [CrossRef]
70. Baker, E.L.; Pham, J.; Vuong, T. *An Empirical Shaped Charge Jet Breakup Model*; Technical Report; ARDEC: Picatinny Arsenal, NJ, USA, 2014.

Disclaimer/Publisher's Note: The statements, opinions and data contained in all publications are solely those of the individual author(s) and contributor(s) and not of MDPI and/or the editor(s). MDPI and/or the editor(s) disclaim responsibility for any injury to people or property resulting from any ideas, methods, instructions or products referred to in the content.